INFORMATION TO USERS

This manuscript has been reproduced from the microfilm master. UMI films the text directly from the original or copy submitted. Thus, some thesis and dissertation copies are in typewriter face, while others may be from any type of computer printer.

The quality of this reproduction is dependent upon the quality of the copy submitted. Broken or indistinct print, colored or poor quality illustrations and photographs, print bleedthrough, substandard margins, and improper alignment can adversely affect reproduction.

In the unlikely event that the author did not send UMI a complete manuscript and there are missing pages, these will be noted. Also, if unauthorized copyright material had to be removed, a note will indicate the deletion.

Oversize materials (e.g., maps, drawings, charts) are reproduced by sectioning the original, beginning at the upper left-hand corner and continuing from left to right in equal sections with small overlaps.

Photographs included in the original manuscript have been reproduced xerographically in this copy. Higher quality 6" x 9" black and white photographic prints are available for any photographs or illustrations appearing in this copy for an additional charge. Contact UMI directly to order.

Bell & Howell Information and Learning
300 North Zeeb Road, Ann Arbor, MI 48106-1346 USA
800-521-0600

Some Fundamental Issues of Constrained Layer Damping Treatments

Yao-Hsin Huang

A dissertation submitted in partial fulfillment of the
requirements for the degree of

Doctor of Philosophy

University of Washington
2000

Program Authorized to Offer Degree: Department of Mechanical Engineering

In presenting this dissertation in partial fulfillment of the requirements for the Doctoral degree at the University of Washington, I agree that the Library shall make its copies freely available for inspection. I further agree that extensive copying of the dissertation is allowable only for scholarly purposes, consistent with "fair use" as prescribed in the U.S. Copyright Law. Requests for copying or reproduction of this dissertation may be referred to Bell and Howell Information and Learning, 300 North Zeeb Road, Ann Arbor, MI 48106-1346, to whom the author has granted "the right to reproduce and sell (1) copies of the manuscript in microform and/or (b) printed copies of the manuscript made from microform."

Signature 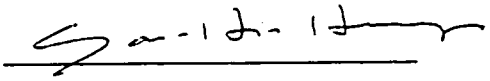

Date 9-25-00

University of Washington

Graduate School

This is to certify that I have examined this copy of a doctoral dissertation by

Yao-Hsin Haung

and have found that it is complete and satisfactory in all respects,
and that any and all revisions required by the final
examining committee have been made.

Chair of Supervisory Committee:

Per G. Reinhall

Reading Committee:

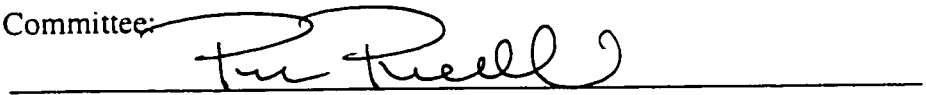

Per G. Reinhall

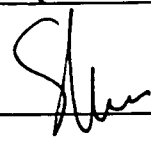

I.Y. (Steve) Shen

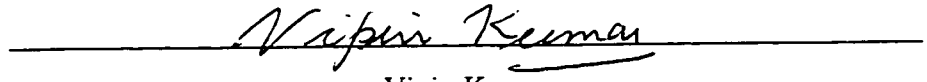

Vipin Kumar

Date: 9-25-2000

University of Washington

Abstract

Some Fundamental Issues of Constrained Layer Damping Treatments

Yao-Hsin Huang

Chairperson of the Supervisory Committee:
Associate Professor Reinhall, Per G.
Department of Mechanical Engineering

Constrained layer damping (CLD) treatment is a widely used surface damping treatment for controlling vibration and noise. The most commonly used mathematical formulation for a beam with the CLD treatment was developed by Mead and Markus. In their formulation, the longitudinal displacements of the base beam and the constraining layer are assumed to be dependent. As a result, the Mead-Markus formulation only applies for some boundary conditions. In the first issue, the error of the Mead-Markus formulation was investigated as a function of the thickness of viscoelastic layer and was shown to be large for certain common boundary conditions. A modified Mead-Markus formulation that allows the longitudinal motion of the base beam and constraining layer to be independent is suggested as a remedy.

The second issue in the dissertation is a study of thickness deformation of the viscoelastic material in CLD treatments. The first goal is to confirm experimentally that thickness deformation exists. The experimental results showed that our experimental method is able to measure thickness deformation as low as 0.5%. We found that thickness deformation increases as thickness of the viscoelastic layer increases. In addition, partial treatments tend to have larger thickness deformation than full treatments. The second goal is to evaluate the accuracy of a mathematical model developed by Miles and Reinhall that accounts for thickness deformation. Comparisons of the numerical results with the experimental measurements indicated that consideration of thickness deformation can improve the accuracy of existing constrained layer damping models when the thickness deformation is noticeable.

In the third issue, with a goal of reducing the weight penalty of CLD treatments, two feasibility studies were conducted to investigate the use of microcelullar foam as damping and standoff layer material. Modified polyethylene teraphthalate (PETG) microcellular foam was used in our studies. Our results show that the loss factor of PETG foam with densities from 42 kg/m^3 to 240 kg/m^3 is in the range of 2% to 8%. In addition, use of microcellular foam as standoff layer can reduce vibration amplitude up to 80% with only a 2 % to 3% weight penalty.

TABLE OF CONTENTS

LIST OF FIGURES

LIST OF TABLES

ACKNOWLEDGEMENTS

Sincere thanks go to my advisor Professor Reinhall and my co-advisor Professor Shen, not only for their direction and guidance of my research, but also for the tremendous encouragement and support I received from them. Words cannot express how much I appreciate the many hours they spent patiently discussing research issues with me. Appreciation also goes to Professor Kumar and Professor Garbini for serving on my advisory committee. In addition, I wish to thank Professor Kumar for giving me convenient access to his lab.

I am thankful for my parents and sister Sarah for showering verbal encouragements and understanding upon me. I am also grateful for my wife Jean. She played a major role in taking care of the family, especially our first baby Jennifer. Throughout the time that I was working on my research and dissertation, she always stood behind me and helped me maintained a balanced life.

Finally, I acknowledge that without the steadfast promise of the Lord and the faithful prayers of many family members and friends, both near and far, this thesis would not be possible.

I know what is to be in need, and I know what it is to have plenty.
I have learned the secret of being content in any and every situation,
whether well fed or hungry, whether living in plenty or in want.
I can do everything through Him who gives me strength.

Philippians 4:12-13

Chapter 1

INTRODUCTION

1.1 Constrained Layer Damping Treatments

Surface damping treatments have been widely used to reduce vibration amplitude, noise generation, and sound transmission associated with thin structures. These treatments are usually thin, lightweight, and durable. They can be easily applied to existing structures to provide high damping performance over wide temperature and frequency ranges. Surface damping treatments can be classified into two main groups. A treatment that is coated on one or both sides of a structure (as shown in Figure 1.1) is called free layer damping treatment. Whenever the structure is subjected to cyclic bending, the damping material is subjected to tension or compression deformation to dissipate the vibratory energy. If an elastic constraining layer is applied to restrict the free layer damping treatment, the damping material will deform in shear to dissipate vibratory energy. This type of damping treatment is called constrained layer damping treatment (see Figure 1.1). Constrained layer damping (CLD) has been proven to be more effective than free layer damping [1] and is the focus of our research.

CLD treatments have been utilized in many commercial and defense designs. The automotive industries use CLD treatments to reduce vibration in disc and drum brake pads. In the aerospace industry, these treatments provide significant damping in fuselages and wing skin of commercial airplanes. In high-speed computer disk drives, damping treatments have been used to effectively reduce noise and vibration level in the head slider suspension system, circuit board damper, and top cover. In addition, CLD treatments can also be found in consumer products such as appliances, audio equipments, and sports equipments.

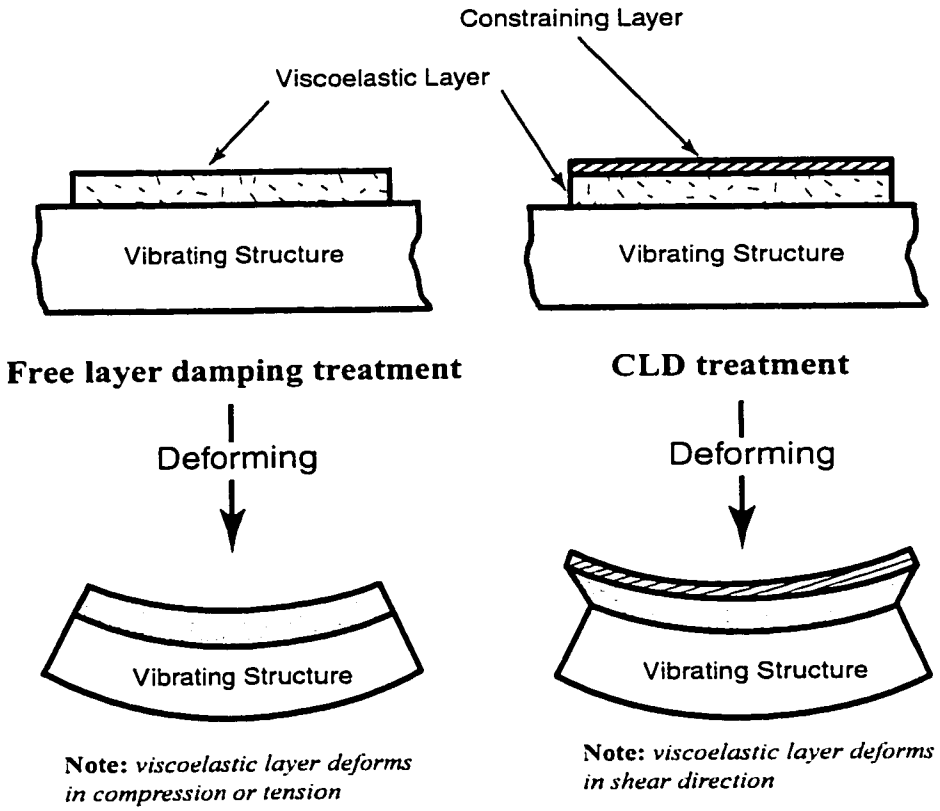

Figure 1.1 Surface damping treatments

1.2 Mathematical Models for Constrained Layer Damping

The concepts of constrained layer damping were introduced by William Swallow in a British patent in 1939 [2]. The fundamental analysis work was developed by Ross, Ungar, and Kerwin [3]. In their research, they treated the problem by assuming (1) a perfect interface between each layer, (2) the same amount of transverse displacement in each layer, (3) damping only from the shearing of the viscoelastic layer, and (4) simply supported boundary conditions. This led to a single fourth order beam equation. DiTaranto [4] extended this analysis to include freely vibrating beams having unspecified boundary conditions. Based on DiTaranto's study and the assumptions made by Ross, Ungar, and Kerwin , Mead and Markus [5] derived an Euler-Bernoulli beam with general boundary conditions and obtained a sixth order equation of motion. We called it the Mead-Markus model. Figure 1.2 shows the displacement variables and dimension fields associated with the Mead-Markus model. The variables representing transverse and longitudinal displacements of the j-th layer are $w_j'(x', t)$ and $u_j'(x', t)$, respectively, where x' is the distance along the beam and t represents time. The subscripts 1, 2 and 3 of the variables indicate the base beam, the viscoelastic layer, and the constraining layer, respectively. The primes indicate that the physical quantities have not been non-dimensionalized. All the layers have length L and width b. Each j-th layer has thickness H_j, density ρ_j, and complex shear moduli E_j^* and G_j^* with corresponding loss factors η_j. (E_j and G_j without the superscript star are the real storage modulus in the equation).

In deriving the Mead-Markus model, the base beam and the constraining layer are assumed to undergo identical transverse displacements represented by $w'(x', t)$. Furthermore, the Mead-Markus model assumes that the longitudinal displacements of the base beam $u'_1(x', t)$ and the constraining layer $u'_3(x', t)$ are dependent through the relation of $E_1 A_1 u'_1 = - E_3 A_3 u'_3$, where $E_1 A_1$ and $E_3 A_3$ are axial rigidities of the base beam and the constraining layer, respectively. This leads to a sixth order equation of motion model that is currently widely applied in most constrained layer damping research:

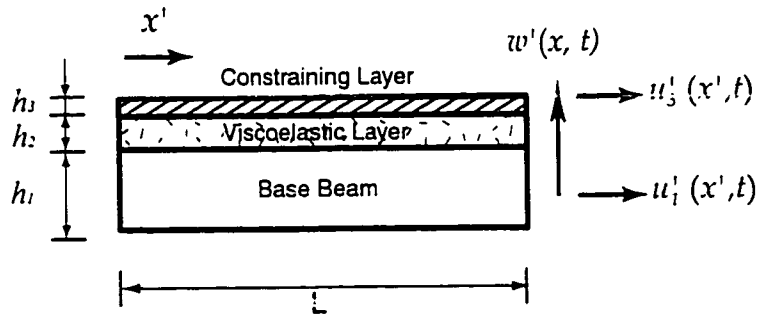

Figure 1.2 Displacement variable fields of the Mead-Markus model

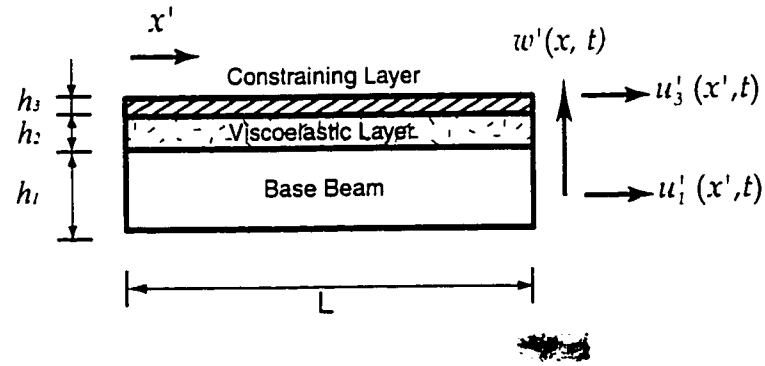

Figure 1.3 Displacement variable fields of the TD model

$$\frac{\partial^6 w'}{\partial x'^6} - (g + \frac{bd^2 G_2}{D_t H_2}) \frac{\partial^4 w'}{\partial x'^4} + \frac{m}{D_t} \frac{\partial^2}{\partial t'^2} (\frac{\partial^2}{\partial x'^2} - g) w' = 0 \qquad (1.1)$$

where

$$g = \frac{G_2 b}{H_2} (\frac{1}{E_1 b H_1} + \frac{1}{E_3 b H_3}), \quad d = \frac{2H_2 + H_1 + H_3}{2}, \quad D_t = \frac{E_1 b H_1^3}{12} + \frac{E_3 b H_3^3}{12}$$

and

$$m = \rho_1 b H_1 + \rho_2 b H_2 + \rho_3 b H_3$$

In the Mead-Markus model, the assumption of $E_1 A_1 u'_1 = - E_3 A_3 u'_3$ limits the boundary conditions on the constraining layer and the base beam. In order to incorporate more selections of boundary conditions, the assumption is sometimes removed resulting in independent u'_1 and u'_3 [6,7]. We called the resulting model the modified Mead-Markus model (MMM).

Although the viscoelastic layer dissipates energy primarily through shear deformation, in some constrained layer designs, the viscoelastic layer may also dissipate energy through thickness deformation. A well-known example is the I-shape constrained layer used in the crown section of the Boeing 747 to eliminate turbulent boundary layer noise. To account for this thickness deformation, Miles and Reinhall [8] extended the Mead-Markus model by assuming that the constraining layer can move both longitudinally and transversely independent of the base beam. In their model, hereafter called the thickness deformation (TD) model, $w'_1(x', t)$ and $w'_3(x', t)$ represent the transverse displacements of the base beam and the constraining layer, respectively (see Figure 1.3). If $w'_1 = w'_3$ is assumed, the TD model reduces to the MMM model. If the longitudinal inertia is neglected and $E_1 A_1 u'_1 = - E_3 A_3 u'_3$ is assumed, the TD model reduces to the original Mead-Markus model.

Other theoretical models considering thickness deformation include Douglas and Yang [9] and Douglas [10], who modeled the viscoelastic layer as a viscoelastic

foundation capable of thickness deformation and performed experiments to demonstrate the existence of thickness deformation. Sylwan [11] and Chen and Sheu [12] modeled the viscoelastic layer by a spring-dashpot system to illustrate the existence of thickness deformation. Austin and Inman [13] analyzed thickness deformation of the viscoelastic layer using the method of modal strain energy.

1.3 Motivation and Objectives

Research on CLD has drawn a lot of attention in recent years. Many researchers have been investigating the effectiveness of CLD with regard to the thickness of the damping layer, the coverage size and the position of CLD relative to the vibrating structure. Some innovative CLD treatments such as standoff CLD have been designed. The application of active signal control and smart materials in CLD are other topics being investigated. In an active constrained layer damping design, a piezoelectric constraining layer replaces the traditional elastic constraining layer so that vibration of signals can be measured, and the resulting signals are then fed back to the piezoelectric constraining layer to control the vibration [7,14,15]. The search for new materials with high damping ratio and the ability to withstand wide-range thermal and intense acoustic and vibratory environments is an on-going effort.

In this dissertation, we studied and evaluated the validity of the mathematical models for CLD. Utilization of microcellular foam materials as damping and standoff layer in CLD was also examined. The following are brief descriptions of the three specific issues we investigated:

- **Issue 1: Analysis of the Mead-Markus model and its boundary conditions**

  The most commonly used equation of motion for a constrained layer damped beam was developed by Mead and Markus. In the formulation of the Mead-Markus model, two important assumptions were made:

1. The thickness deformation of the viscoelastic layer was not considered. The transverse displacement is represented by using only variable w' for both the base beam and the constraining layer.
2. Two axial displacement variables u'_1, and u'_3 were used in the derivation of the equations of motions, but they are dependent. This is because an assumption was made regarding the relationship between u'_1 and u'_3 :

$$u'_1 = -C\,u'_3, \quad C = \frac{E_3 A_3}{E_1 A_1} \tag{1.2}$$

where $E_1\ A_1$ and $E_3\ A_3$ are axial rigidities of the base beam and the constraining layer respectively.

When the assumption of $u'_1 = C\ u'_3$ is made, it automatically limits some boundary conditions. This limitation can be demonstrated, for example, by a cantilevered based beam with free-free constraining layer in a simple lab experimental setup. At the cantilevered end ($x' = 0$), the displacement u'_1 is equal to zero, and according to the assumption, the displacement u'_3 must be zero, too. However, physically, the displacement u'_3 is not necessarily zero. In this case, the axial displacements of the beam u'_1 and the constraining layer u'_3 are independent at the cantilevered end. Therefore, we see that this boundary condition violates the basic assumption of the Mead-Markus model. Alternatively, we can say that the Mead-Markus model cannot define this specific case.

In order to allow for a greater range of boundary conditions, the modified Mead-Markus model (MMM), that assumes the base beam and the constraining layer can move independently in the longitudinal direction [7] was developed. In this model, $u'_1(x', t)$and $u'_3(x', t)$ are independent, and the transverse displacements of the base beam and the constraining layer are identical and

represented by a single field variable w'. In the MMM model, if the inertia associated with the longitudinal motion of the constraining layer and the base beam is neglected, the MMM model can be reduced to the Mead-Markus model.

In this dissertation, we report on a theoretical and experimental analysis of the Mead-Markus and MMM models. First, we show how the analytical frequency response function of the Mead-Markus and MMM models are computed. An investigation into the frequency response functions of the Mead-Markus and MMM models under different boundary conditions are reported. Finally, a description of our experimental setup and results follows. We focus on a specific set of boundary conditions that is excluded by the Mead-Markus model but can be handled by the MMM model.

• **Issue 2: Thickness deformation of constrained layer damping**

Thickness deformation of the viscoelastic layer has been considered an important factor in the modeling of the constrained layer damped beam by many theoretical studies. Results from these research efforts demonstrated the existence and significance of the thickness deformation of the viscoelastic layer. Despite these theoretical research results, there are reasons for pursuing a more thorough study in this area. First, previously used techniques to obtain thickness deformation have not employed direct measurements; therefore, thickness deformation could not be detected unless it far outweighed the shear deformation. For example, Douglas and Yang [9] measured mechanical impedances of the base beam and compared the impedances with theoretical predictions that assumed only thickness deformation and no shear deformation. The thickness deformation was not measured directly. Instead, agreement of the experimental and theoretical results indicated the existence of thickness deformation. Lack of direct measurements implies that thickness deformation cannot be quantified accurately for a given constrained layer design. Second, the 12th-order TD model has never been compared with experimental data and has not been used to calculate

frequency response functions (FRFs) numerically. The computation of FRFs is essential in assessing the contribution of the thickness deformation. After the FRFs are computed, the assumption of thickness deformation can then be evaluated by comparing with the MMM model.

Development of an experimental technique for direct measurement and obtaining numerical solutions for the TD model can help answer several important questions lingering in the damping community regarding thickness deformation. These include: Does thickness deformation become significant for a constrained layer treatment with a thin viscoelastic layer undergoing primarily shear deformation? For a given constrained layer design, how much energy dissipation will result from shear or thickness deformation? In order to answer these questions, we first confirm the existence of thickness deformation through direct measurements. Secondly, the accuracy of the TD model is evaluated by calculating the frequency response functions using the method of distributed transfer functions [16]. The theoretical predictions of the TD model are compared with results from the experiments and the MMM model.

• **Issue 3: Utilization of microcellular foam materials in CLD**

In designing CLD treatments, there are several factors to consider. First, the effectiveness of CLD treatments are often limited by the thermal environment that the structure is designed to operate in. Most viscoelastic materials have their highest loss factor in a limited temperature range, i.e., the glass transition temperature. Therefore, materials with significant loss factor over a wide temperature range are highly desirable. The second factor in CLD design is weight penalty. It is desirable to minimize the increase in weight due to the viscoelastic, standoff and constraining layers.

Microcellular foams commonly refer to closed-cell thermoplastic foams that have bubble diameters in the range of 5 to 50 micrometers and bubble densities exceeding 10^8 bubbles per cubic centimeter. Because the foam material consists

of a large number of bubbles, the density of the foam becomes relatively low. In this regard, microcellular foams present many desirable features for CLD treatments. For example, it is light-weighted so it can be used in CLD as damping or standoff layer without incurring high penalty. The internal foam structure might be engineered to create different degrees of damping. In this issue, we study the feasibility of using microcellular foam in CLD applications. PETG microcellular foam is used as our testing specimen. The first feasibility study is to use microcellular foam as a damping layer in CLD. Two foam configurations were tested: uncompressed and compressed. To evaluate the damping performance, shear storage modulus and loss factor of the foams were measured following ASTM standard E756-80. The tests were repeated for foams with different densities. The second feasibility study is to use microcellular foam as a standoff layer. The damping performance of a CLD beam with different foams as the standoff layer was investigated, and the corresponding weight penalty is discussed.

1.4 Organization

The dissertation is organized into three main parts. Chapter 2 focused on the boundary conditions of the CLD beam and the Mead-Markus model. In chapter 3, we considered the behavior of thickness deformation in the CLD beam. The utilization of microcellular foam materials in CLD was investigated and discussed in chapter 4. Finally, chapter 5 contains conclusions of the dissertation and suggestions for future work.

Chapter 2

AN ANAYSIS OF THE MEAD-MARKUS MODEL AND ITS BOUNDARY CONDITIONS

The most commonly used beam model for constrained layer damping was developed by Mead and Markus [1]. In the model, three displacement variables were used but only two of them were independent. As a result, the Mead-Markus formulation only applies to a class of systems with boundary conditions described in Markus et al. [20], Rao [21], and Lifshitz and Leibowitz [22]. In this chapter, we first illuminate where the deficiency occurs and then propose a possible remedy. We report on a theoretical and experimental analysis of the Mead-Markus and the MMM models and show how the analytical frequency response function of the MMM model is computed. An investigation into the frequency response functions of the Mead-Markus model under some specific boundary conditions is reported. Finally, a description of our experimental setup and results follows. We focus on a specific set of beam boundary conditions which is frequently used in CLD research.

2.1 Limitations of the Mead-Markus Model

Figure 2.1 shows the displacement variable fields associated with the Mead-Markus model for an Euler-Bernoulli beam. The transverse displacement is represented by $w'(x', t)$, and longitudinal displacement of the j-th layer is represented by $u'_j(x', t)$, where x is the position along the beam and t is time. The subscripts 1, 2 and 3 refer to the base beam, the viscoelastic layer, and the constraining layer, respectively. All the layers have length L and width b. The j-th layer has thickness h_j, and storage moduli

E_j and G_j. In the Mead-Markus model, assuming equilibrium of axial force P_1 on the base beam and axial force P_2 on the constraining layer results in

$$E_1 h_1 b \frac{\partial u_1'}{\partial x} = -E_3 h_3 b \frac{\partial u_3'}{\partial x} \tag{2.1}$$

where $E_1 h_1 b$ and $E_3 h_3 b$ are axial rigidities of the base beam and the constraining layer, respectively. Integration of equation (2.1) with respect to x leads to equation (8) of Mead and Markus [1], i.e.,

$$E_1 h_1 u_1' = -E_3 h_3 u_3' \quad \text{or} \quad u_1' = -\frac{E_3 h_3}{E_1 h_1} u_3' \tag{2.2}$$

Note that u_1 and u_3 are no longer independent in equation (2.2) after the integration.

The presence of equation (2.2) has several profound implications. First, the dependence of u'_1 and u'_3 limits the boundary conditions allowed in the Mead-Markus formulation as shown in the following two examples. Example in Figure 2.1 illustrates a simple lab setup consisting of a cantilevered base beam and a free-free constraining layer. The proper boundary conditions at the left end should be

$$\frac{\partial u_1'(0,t)}{\partial x'} = 0 \quad \text{and} \quad u_3'(0,t) = 0 \tag{2.3}$$

which implies that $u'_1(0, t) \neq 0$ for the free-free constraining layer and violates the assumption made in equation (2.2) [6]. A more explicit example is the active system shown in Figure 2.2. A piezoelectric material is added between the constraining layer and the fixed wall at $x' = 0$. In addition, the displacement of the piezoelectric material is controlled by an external source $p(t)$. Therefore, the proper boundary conditions are

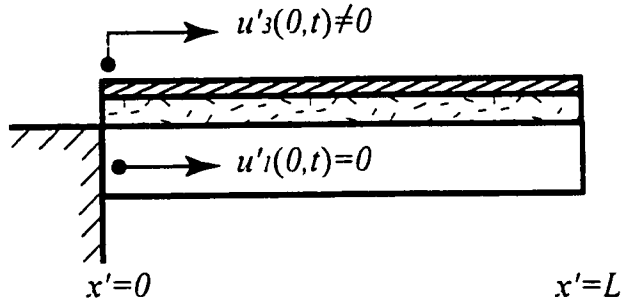

Figure 2.1 An exmple of passive CLD treatment of violation of the Mead-Markus model

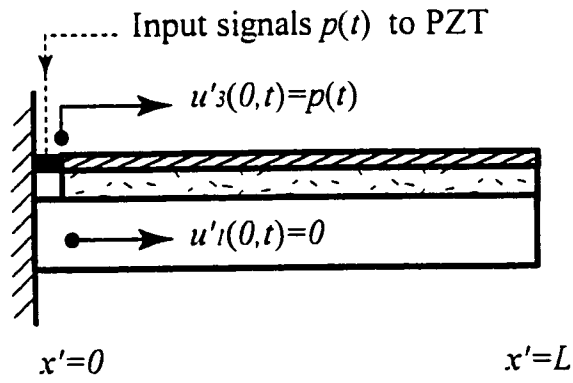

Figure 2.2 An exmple of active CLD treatment of violation of the Mead-Markus model

$$u_1'(0,t) = p(t) \quad \text{and} \quad u_3'(0,t) = 0 \tag{2.4}$$

which obviously violate the assumption made in equation (2.2).

To incorporate the boundary conditions described in equation (2.3) or (2.4), one needs to understand that u'_1 and u'_3 are mathematically independent. The integration of equation (2.1) should result in

$$u_1'(x) = -\frac{E_3 h_3}{E_1 h_1} u_3'(x) + C \tag{2.5}$$

where C is not necessarily zero and takes the form

$$C = -\frac{E_3 h_3}{E_1 h_1} u_3'(\xi) + u_1'(\xi) \tag{2.6}$$

with ξ being an arbitrary point along the beam.

2.2 Theoretical Analysis

In the Mead-Markus model, the assumption of $E_1 A_1 u'_1 = - E_3 A_3 u'_3$ limits the boundary conditions on the constraining layer and the base beam. In order identify cases where this assumption made in the Mead-Markus model is valid, we investigated the frequency responses obtained from the Mead-Markus model with those obtained fromthe MMM model [7], which allows the base beam and the constraining layer to move independently in the longitudinal direction. In the MMM model, $u'_1(x', t)$and $u'_3(x', t)$ are independent, and the transverse displacements of the base beam and the constraining layer are identical and represented by a single field variable w'. Using the

same field variables and parameters as described in section 1.2.1, the following are the three equations of motion for the MMM model:

$$\left(\frac{E_1^* bH_1^3}{12}+\frac{E_3^* bH_3^3}{12}\right)\frac{\partial^4 w'}{\partial x'^4}-G_2^* bH_2\left[1+\frac{H_1+H_3}{H_2}+\left(\frac{H_1+H_3}{2H_2}\right)^2\right]\frac{\partial^2 w'}{\partial x'^2} + m\frac{\partial^2 w_1'}{\partial t'^2}-\frac{G_2^* b}{2H_2}(H_1+2H_2+H_3)\left(\frac{\partial u_1'}{\partial x'}-\frac{\partial u_3'}{\partial x'}\right)=0 \tag{2.7}$$

$$(\rho_1 bH_1)\frac{\partial^2 u_1'}{\partial t'^2}-E_1^* bH_1\frac{\partial^2 u_1'}{\partial x'^2}+\frac{G_2^* b}{H_2}(u_1'-u_3')+\frac{G_2^* b}{2H_2}(2H_2+H_1+H_3)\frac{\partial w'}{\partial x'}=0 \tag{2.8}$$

$$(\rho_3 bH_3)\frac{\partial^2 u_3'}{\partial t'^2}-E_3^* bH_3\frac{\partial^2 u_3'}{\partial x'^2}-\frac{G_2^* b}{H_2}(u_1'-u_3')-\frac{G_2^* b}{2H_2}(2H_2+H_1+H_3)\frac{\partial w'}{\partial x'}=0 \tag{2.9}$$

If equation (2.8) and (2.9) are added together and the longitudinal inertia is neglected, and then substitute into equation (2.7), the MMM model can be reduced to the original Mead-Markus model without the applied loading.

2.2.1 Solving Equations of Motion for the MMM model

The frequency responses given by these two models were computed by using the distributed transfer function method developed by Yang and Tan [16]. Here we show the procedure to obtain frequency response function (FRF) for the MMM model.

First, the field variables in the equations of motion and the boundary conditions are non-dimensionalized in the Laplace transform domain by the following relations:

$$x=\frac{x'}{L},\quad s=s'\sqrt{\frac{L^4\rho}{D_1^*}},\quad \text{where } \rho=\rho_1+\rho_2+\rho_3$$

$$w(x,s)=\frac{\bar{w}'(x',s')}{H_1},\quad u_1(x,s)=\sqrt{\frac{L^2 bH_1E_1}{D_1H_1^2}}\,\bar{u}_1(x,s),\quad u_3(x,s)=\sqrt{\frac{L^2 bH_1E_1}{D_1H_1^2}}\,\bar{u}_3(x,s)$$

The field variables $\bar{w}'(x',s')$, $\bar{u}'_1(x',s')$, and $\bar{u}'_3(x',s')$ are the Laplace transform of $w'(x',t')$, $u'_1(x',s')$, and $u'_3(x',s')$. The normalized equations of motion can then be expressed in matrix form in the Laplace transform domain as:

$$\left\{\begin{bmatrix} D_t^* \dfrac{\partial^4}{\partial x^4} + s^2 & 0 & 0 \\ 0 & -E_3^* \dfrac{\partial^2}{\partial x^2} + s^2\alpha_3^2 & 0 \\ 0 & 0 & -E_1^* \dfrac{\partial^2}{\partial x^2} + s^2\alpha_1^2 \end{bmatrix} + \varepsilon \begin{bmatrix} \dfrac{-\partial^2}{\partial x^2} & -\beta_{12}\dfrac{\partial}{\partial x} & \beta_{13}\dfrac{\partial}{\partial x} \\ \beta_{12}\dfrac{\partial}{\partial x} & \beta_{12}^2 & -\beta_{12}\beta_{13} \\ -\beta_{13}\dfrac{\partial}{\partial x} & \beta_{12}\beta_{13} & \beta_{13}^2 \end{bmatrix}\right\} \begin{Bmatrix} w(x,s) \\ u_3(x,s) \\ u_1(x,s) \end{Bmatrix} = \begin{Bmatrix} 0 \\ 0 \\ 0 \end{Bmatrix} \tag{2.10}$$

where

$$\varepsilon = \frac{G_2 b d^2 H_2 L^2}{D_t}, \quad D_t^* = \left(\frac{bH_1^3}{12}E_1^* + \frac{bH_3^3}{12}E_3^*\right)/D_t$$

$$\beta_{12} = \frac{1}{dH_2}\sqrt{\frac{D_t}{bH_3E_3}}, \quad \beta_{13} = \frac{1}{dH_2}\sqrt{\frac{D_t}{bH_1E_1}}, \quad \alpha_1^2 = \frac{\rho_1}{\rho}\frac{D_t}{bH_1E_1L^2}, \quad \alpha_3^2 = \frac{\rho_3}{\rho}\frac{D_t}{bH_3E_3L^2}$$

The equations of motion can be expressed in state space form as

$$\frac{dy(x,s)}{dx} = F(s)\cdot y(x,s) \tag{2.11}$$

where

$$y(x,s) = \left\{w, \frac{dw}{dx}, \frac{d^2w}{dx^2}, \frac{d^3w}{dx^3}, u_3, \frac{du_3}{dx}, u_1, \frac{du_1}{dx}\right\}^T \tag{2.12}$$

$$F(s)=\begin{bmatrix} 0 & 1 & 0 & 0 & 0 & 0 & 0 & 0 \\ 0 & 0 & 1 & 0 & 0 & 0 & 0 & 0 \\ 0 & 0 & 0 & 1 & 0 & 0 & 0 & 0 \\ \dfrac{-s^2}{D_t^n} & 0 & \dfrac{\varepsilon}{D_t^n} & 0 & 0 & \dfrac{\varepsilon\beta_{12}}{D_t^n} & 0 & \dfrac{-\varepsilon\beta_{13}}{D_t^n} \\ 0 & 0 & 0 & 0 & 0 & 1 & 0 & 0 \\ 0 & \dfrac{\varepsilon\beta_{12}}{E_3^n} & 0 & 0 & \dfrac{\varepsilon\beta_{12}^2+s^2\alpha_3^2}{E_3^n} & 0 & \dfrac{-\beta_{12}\beta_{13}\varepsilon}{E_3^n} & 0 \\ 0 & 0 & 0 & 0 & 0 & 0 & 0 & 1 \\ 0 & \dfrac{-\varepsilon\beta_{13}}{E_1^n} & 0 & 0 & \dfrac{-\beta_{12}\beta_{13}\varepsilon}{E_1^n} & 0 & \dfrac{\varepsilon\beta_{13}^2+s^2\alpha_1^2}{E_1^n} & 0 \end{bmatrix}$$

The normalized boundary conditions can also be expressed in state space form as

$$M(s)\underline{y}(0,s)+N(s)\underline{y}(1,s)=g(s) \tag{2.13}$$

where

$$g(s)=\{P(s).0.0.0.0.0.0.0.0.0\}^T \tag{2.14}$$

For the boundary conditions of a cantilevered base beam with free-free constraining layer as mentioned in example (1) in Figure 2.2, the M and N in (2.13) is

$$M(s)=\begin{bmatrix} 1 & 0 & 0 & 0 & 0 & 0 & 0 & 0 \\ 0 & 1 & 0 & 0 & 0 & 0 & 0 & 0 \\ 0 & 0 & 0 & 0 & 0 & 0 & 1 & 0 \\ 0 & 0 & 0 & 0 & 0 & 1 & 0 & 0 \\ 0 & 0 & 0 & 0 & 0 & 0 & 0 & 0 \\ 0 & 0 & 0 & 0 & 0 & 0 & 0 & 0 \\ 0 & 0 & 0 & 0 & 0 & 0 & 0 & 0 \\ 0 & 0 & 0 & 0 & 0 & 0 & 0 & 0 \end{bmatrix} \quad \text{and} \quad N(s)=\begin{bmatrix} 0 & 0 & 0 & 0 & 0 & 0 & 0 & 0 \\ 0 & 0 & 0 & 0 & 0 & 0 & 0 & 0 \\ 0 & 0 & 0 & 0 & 0 & 0 & 0 & 0 \\ 0 & 0 & 0 & 0 & 0 & 0 & 0 & 0 \\ 0 & 0 & 1 & 0 & 0 & 0 & 0 & 0 \\ 0 & 0 & 0 & 0 & 0 & 0 & 0 & 1 \\ 0 & \dfrac{\varepsilon}{D_t^n} & 0 & -1 & \dfrac{\varepsilon\beta_{12}}{D_t^n} & 0 & \dfrac{\varepsilon\beta_{13}}{D_t^n} & 0 \\ 0 & 0 & 0 & 0 & 0 & 1 & 0 & 0 \end{bmatrix}$$

$P(s)$ in (2.14) is the displacement excitation. The solution of (2.11) under boundary conditions (2.13) is

$$y(x,s) = e^{F(s)x} \cdot A^{-1}(s) \cdot g(s) \tag{2.15}$$

where

$$A(s) = M(s) + N(s) \cdot e^{F(s)} \tag{2.16}$$

The transverse displacement w is the first element of y (x, s) as expressed in (2.12). Equation (2.15) can be evaluated at the cantilevered end (x = 0) and the free end (x = 1). We can then obtain the normalized transfer function w (1,s) / w (0,s).

2.2.2 Theoretical Results

Seven theoretical beam FRFs simulation were investigated. Their boundary conditions are the combinations from six different cases as shown in Table 2.1. The dimensions and properties of each layer in the CLD beam are listed in Table 2.2. In the analytical simulation, the storage modulus and the loss factor of the viscoelastic material were obtained from the experimental data presented by Soovere and Drake [23]. The Poisson ratio for the viscoelastic layer was assumed to be a constant 0.45. The loss factors η_1 and η_3 of the untreated aluminum beam were extracted experimentally.

The FRFs of case A in Figure 2.3 show that there is no difference between these two models since the Clamped (2) boundary condition makes the longitudinal motion of the constraining layer and the base beam zero at the fixed end. It does not violate the assumption of $E_1 h_1 u_1' = -E_3 h_3 u_3'$ made in the Mead-Markus formulation. However, if we change the boundary conditions to that mentioned in the first example (case B), the Mead-Markus model becomes insufficient to define the boundary conditions. In order to define the Clamped (1) boundary conditions in the Mead-Markus formulation,

Table 2.1 Boundary conditions of CLD beam

Boundary Conditions		Mathematical Models						
x' → $w'(x',t)$ Constraining Layer Base Beam → $u_3(x',t)$ → $u_1'(x',t)$		The Mead-Markus Model			The MMM Model			
Free	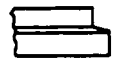	P = 0	M = 0	S = 0	$\frac{\partial u_1'}{\partial x'}=0$	$\frac{\partial u_3'}{\partial x'}=0$	M = 0	S = 0
Clamped-1		Undefined			$w'=0$	$\frac{\partial w'}{\partial x'}=0$	$u_1'=0$	$\frac{\partial u_3'}{\partial x'}=0$
Clamped-2	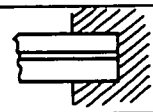	$w'=0$	$\frac{\partial w'}{\partial x'}=0$	= 0	$w'=0$	$\frac{\partial w'}{\partial x'}=0$	$u_1'=0$	$u_3'=0$
Pinned -1		Undefined			$w'=0$	$u_1'=0$	$\frac{\partial u_3'}{\partial x'}=0$	M = 0
Pinned-2		$w'=0$	P = 0	M = 0	$w'=0$	$\frac{\partial u_3'}{\partial x'}=0$	$\frac{\partial u_3'}{\partial x'}=0$	M = 0

P : Axial Force M : Bending Moment S : Shear Force :Shear Stress in the VEM

Table 2.2 Dimension and properties of the test CLD beam

Specimen 1	Base beam	Viscoelastic layer	Constraining layer
Length (mm)	150	150	150
Width (mm)	12	12	12
Thickness (mm)	2.2	0.75	0.80
Material	Al 2024	ISD 112	Al 2024
Modulus (MPa)	E: 69000	G: 0.1 ~ 0.6	E: 69000
Loss Factor (%)	0.03 ~ 0.01	30 ~ 110	0.03 ~ 0.01
Mass density (Kg/m^3)	2700	1060	2700

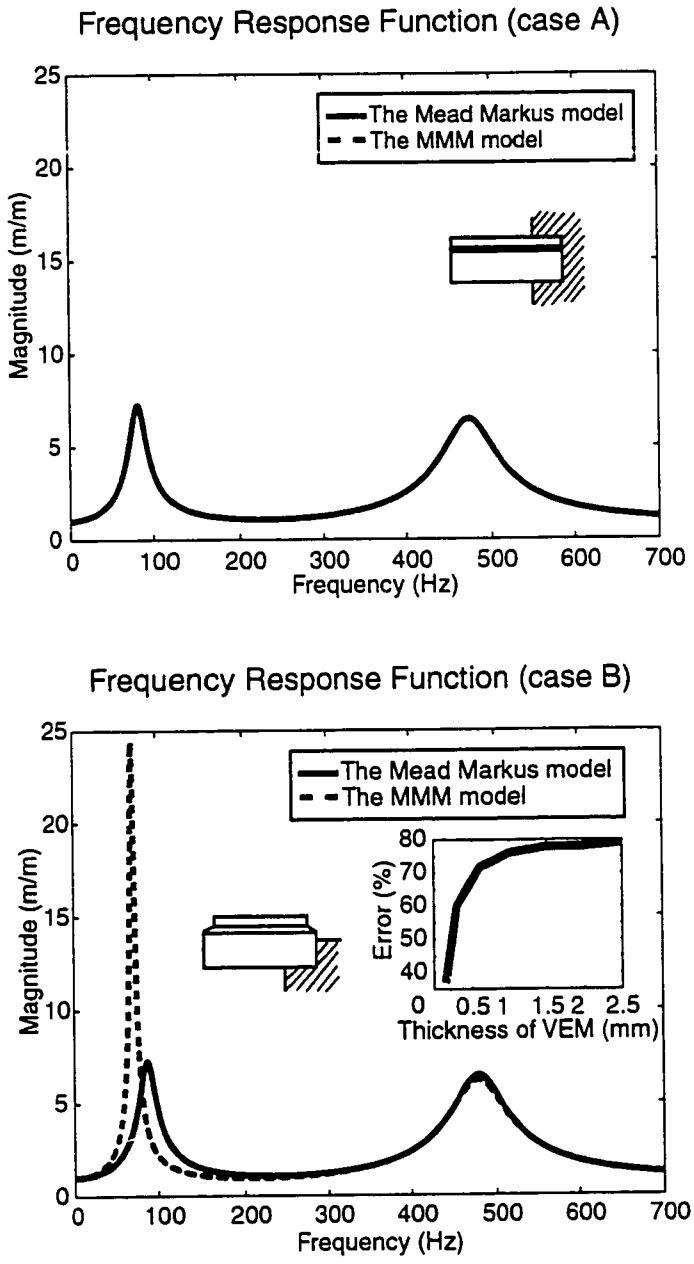

Figure 2.3 Theoretical analysis of cases A and B

the best available option is to use Clamped (2) boundary conditions. This assumption to replace the boundary conditions of Clamped (1) by those of Clamped (2) in the Mead-Markus model might cause some discrepancies between the FRFs from these two models as shown by case B in Figure 2.2. From the theoretical results, the FRFs predicted from these two models are identical except for the first mode where the resonant frequency obtained from the MMM model is lower than the one from the Mead-Markus model. A big difference is also observed in the amplitude. The error from the amplitude difference increases as the thickness of the viscoelastic layer material (VEM) layer increases.

Case C in Figure 2.4 shows the Clamped (2) – Clamped (2) boundary conditions. We analyzed the FRFs from the left (fixed) end to the beam center. There is no problem for the Mead-Markus model to define the boundary conditions in case C. However, the model cannot define case D and case E boundary conditions. Again, case C becomes the best way to model cases D and E in the Mead-Markus model. The results show a difference in amplitude at the first mode and the errors increase when VEM becomes thinner. We also investigated the two cases shown in Figure 2.5. The pinned ends in case G allowed the base beam to move axially. Our examples demonstrate the insufficient ability of the Mead-Markus mode in formulating some specific boundary conditions, resulting in some possible errors. Note there is no appreciable difference between the two formulations at mode 2 or higher for cases D, E, and G.

2.3 Experimental Analysis

In order to verify the difference shown in the theoretical results, we experimentally evaluated case B which shows the significant diversity between the Mead-Markus and the MMM models. Figure 2.6 shows a schematic drawing of our experimental setup. The specimen was constructed by laminating a viscoelastic layer and a constraining layer to a base beam. The configurations are shown in Table 2.2. The specimen was

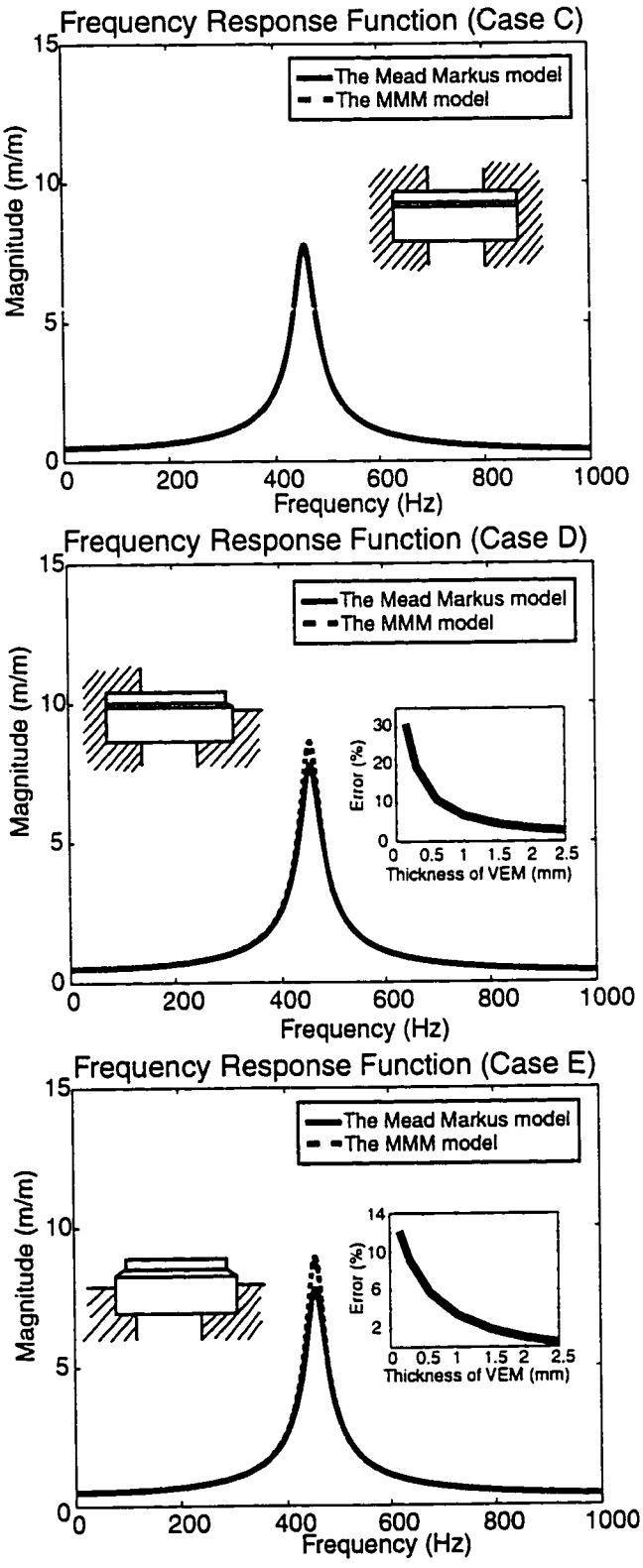

Figure 2.4 Theoretical analysis of cases C, D, and E

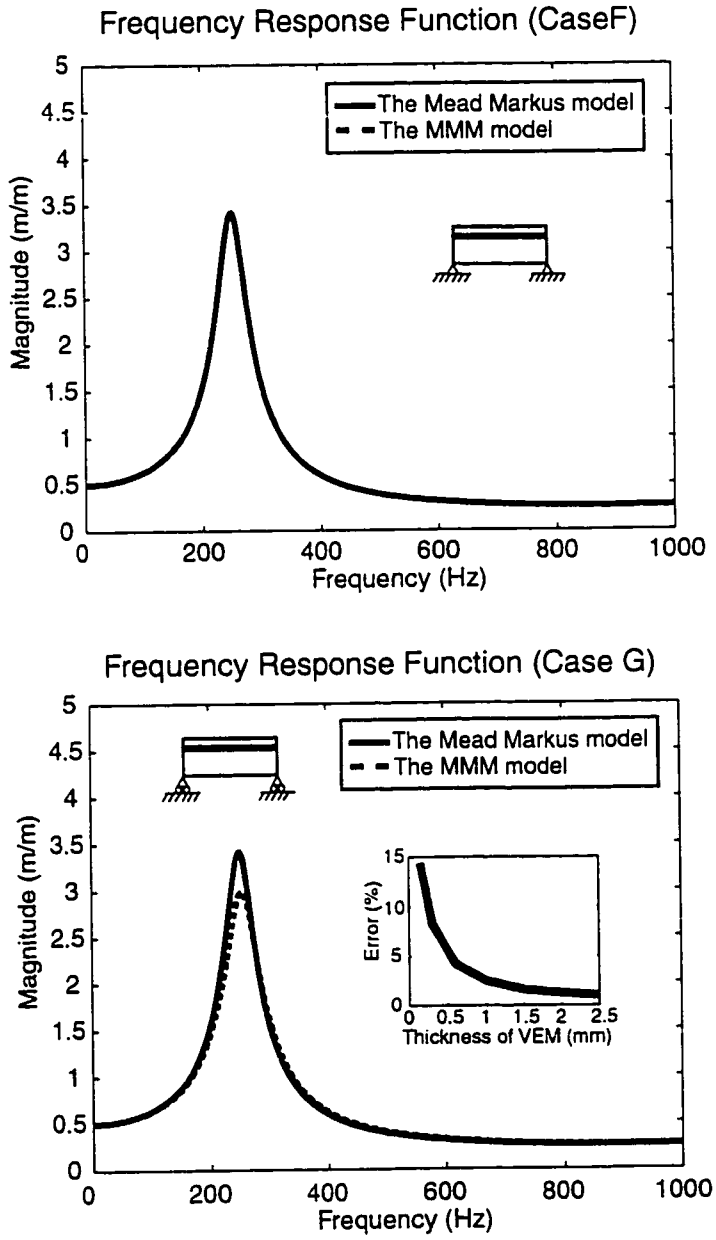

Figure 2.5 Theoretical analysis of cases F and G

cantilevered at its base to a shaker with all ends of the viscoelastic and constraining layers remaining free. A signal generator powers the shaker with Gaussian broadband noise. An accelerometer was mounted at the base beam's cantilevered end to measure the excitation of the specimen's cantilevered end, and a laser vibrometer was used to measure the response of the specimen's free end. The laser vibrometer and the accelerometer were connected to a spectrum analyzer. Because the shear modulus is sensitive to temperature variations, the ambient temperature was maintained at 68°F. In our experiments, we observed the behavior of the first mode. In order to obtain high resolution of the frequency response function, the frequency range was set from 60 Hz to 80 Hz, and the average times for signals collecting was set to be 20 times.

Some calibration tasks were carried out before the actual experiments were conducted. These tasks include self-calibration between the accelerometer and the vibrometer. The location for placing the accelerometer on the shaker armature was also examined. The test results showed that the placement location of the accelerometer does not affect the frequency response of the beam.

The frequency response was obtained by computing the transfer function between the vibrometer and accelerometer outputs. During the experiments, the acceleration $\frac{\partial^2}{\partial t^2} w'(0, t)$ of the cantilevered end and the velocity $\frac{\partial}{\partial t} w'(0, t)$ of the free end were monitored. Then the spectrum analyzer calculated the frequency response function of the specimen $W'(\omega')=W'(L, \omega')/W'(0, \omega')$ where ω' is the frequency, and $W'(x', \omega')$ are the Fourier spectrum of $w'(x', t')$. The coherence of the input and output signals was also monitored to ensure that reasonable results were obtained.

Figure 2.7 shows the comparison of the experimental results and theoretical predictions for mode 1. The peak of the magnitude and the natural frequency from the theoretical prediction by the Mead-Markus model is 7.2 m/m and 88 Hz. The peak of the magnitude and the natural frequency from the MMM model prediction is 24 m/m and 71 Hz. The MMM model predictions are very close to the experimental results(18.5 m/m for the peak magnitude and 68.38 Hz for the natural frequency). Our

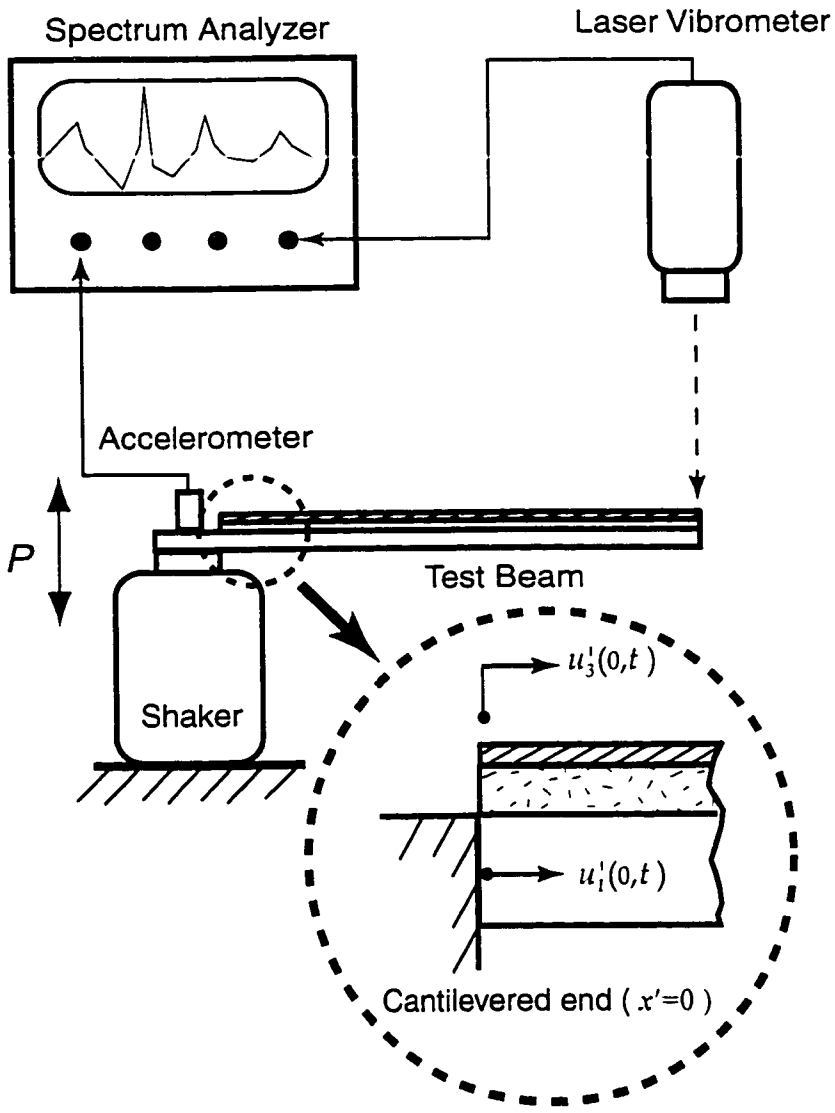

Figure 2.6 Experimental analysis of case B

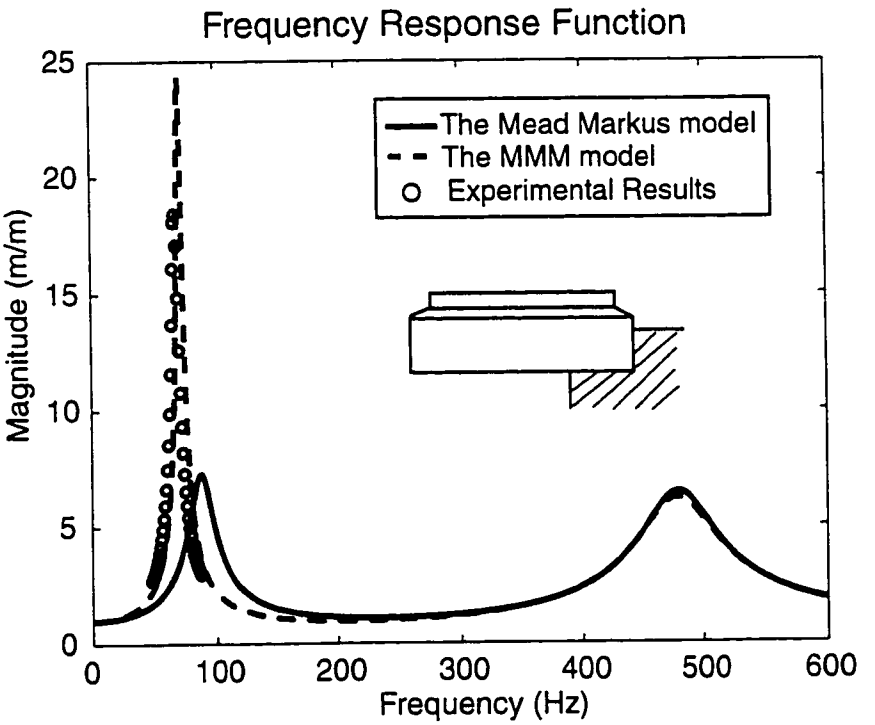

Figure 2.7 Experimental FRFs of case B

results show that the MMM model can accurately predict the vibration behavior of the constrained layer damped beam.

2.4 Conclusions

In this chapter, the limitations of the Mead-Markus model was demonstrated both theoretically and experimentally. We note that careful attention to the boundary conditions must be exercised when predicting the behavior of the first mode using the Mead-Markus model. For certain boundary conditions more accurate results can be obtained by using the MMM model.

Chapter 3

THICKNESS DEFORMATION OF CLD: AN EXPERIMENTAL AND THEORETICAL EVALUATION

This chapter presents a study of thickness deformation of the viscoelastic material in constrained layer damping treatments. The first goal of the study is to confirm experimentally through direct measurements that thickness deformation exists. The second goal is to evaluate the accuracy of a mathematical model developed by Miles and Reinhall [8] also called the TD model, that accounts for thickness deformation. FRFs were calculated by using the method of distributed transfer functions by Yang and Tan [16].

3.1 Experimental Setup and Procedure

Figure 3.1 shows the experimental setup. The constrained layer specimen was cantilevered at its base to a shaker with all ends of the viscoelastic and constraining layers remaining free. The shaker was driven by a signal generator with Gaussian broad band noise. An accelerometer mounted at the base beam's cantilevered end measured the input excitations from the shaker. Two laser vibrometers measured the response of the free end of the base beam and the constraining layer simultaneously. Both the shaker and the laser vibrometers were mounted on an isolation table. A spectrum analyzer computed the FRFs between the accelerometer inputs and the vibrometer outputs. To obtain high resolution, the zoom function was used to measure the FRF mode by mode. The coherence of the signals was monitored throughout the experiments. The ambient temperature was maintained at 68°F since the storage modulus of the viscoelastic material is sensitive to temperature variations.

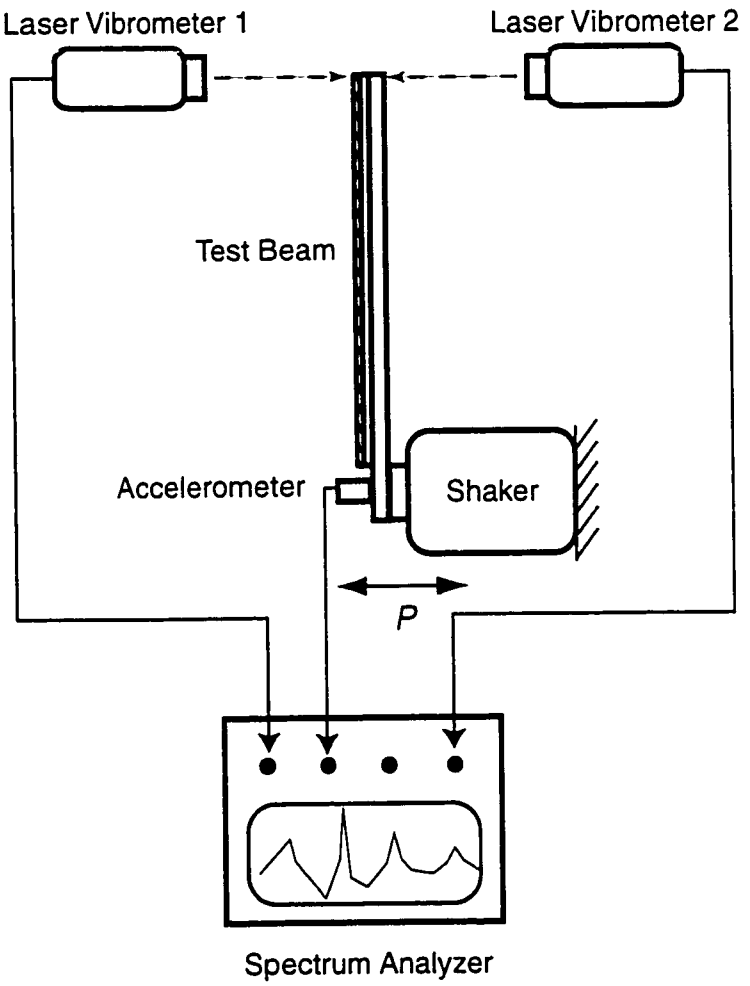

Figure 3.1 Schematic drawing of experimental setup

Three groups of constrained layer damped beams were tested. Group 1 was fully treated, and groups 2 and 3 were partially treated. Table 3.1 lists the dimensions and configurations of the specimens for each group. The specimens in group 2 have longer partial damping treatments than those from group 3, so that thickness deformation of different sizes of damping treatments could be evaluated. In Table 3.1, E indicates the cantilevered end and M indicates the measuring point. In addition, for each group, three specimens (#1, #2, and #3) with different thickness of viscoelastic layers were fabricated so that the thickness deformation of "thin" to "thick" viscoleastic layers could be investigated. Table 3.1 lists the dimensions and material properties that were the same for all three specimen groups, such as the beam width and complex modulus. For the rest of this chapter, the subscript AB in S_{AB} refers to the specimen number B in Group A. In setting up the experiment, several design issues were considered. These included clamping condition, thickness of viscoelastic layers, single vs. double cantilever designs, measurement details, and vibrometer calibration. These issues are explained in detail as follows.

- **Clamping:** To simulate the fixed-end boundary condition, a pair of aluminum brackets sandwiching the base beam were bolted to the shaker. Figure 3.2 shows a schematic drawing of the clamp. Note that the brackets did not clamp the constraining layer or the viscoelastic layer. Clamping those layers would have produced significant deformation of the viscoelastic layer. Moreover, the deformation of the soft viscoelastic layer would make the boundary condition significantly different from a fixed end. Because the chosen clamping condition (Figure 2.2) violates the Mead-Markus assumption $E_1 A_1 u'_1 = - E_3 A_3 u'_3$ [6], the experimental results could only be used to validate the MMM model.

- **Thickness of Viscoelastic Layer:** Specimens #2 and #3 in every group have viscoelastic layers that are thicker than commercially available products. These thicker viscoelastic layers were fabricated by stacking 3M ISD 112 products (20

Table 3.1 Dimensions and the material properties of specimens in each group

Specimen	Base beam	Viscoelastic layer		Constraining layer
Width	*12* mm	*12* mm		*12* mm
Thickness	*2.2* mm	#1	*0.51* mm	0.80 mm
		#2	*1.02* mm	
		#3	*2.04* mm	
Material	Al *2024*	ISD *112*		Al *2024*
Modulus	E: *69000* MPa	G: *0.1 ~ 0.6* MPa		E: *69000* MPa
Loss Factor	*0.29%*	*30 %~ 90%*		*0.29%*
Mass density	*2700* Kg/m^3	*1060* Kg/m^3		*2700* Kg/m^3

Table 3.2 Configurations and dimensions of specimen groups

Group	Group 1	Group 2	Group 3
Configuration	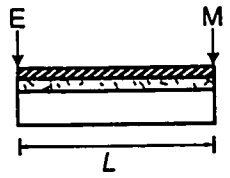	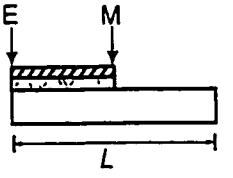	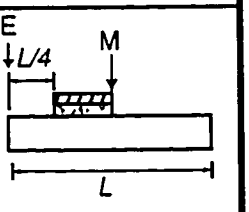
Base beam length (*L*)	*150* mm	*150* mm	*150* mm
Viscoelastic layer length	*150* mm	*75* mm = *L/2*	*36.5* mm = *L/4*
Constraining layer length	*150* mm	*75* mm = *L/2*	*36.5* mm= *L/4*

(E: cantilevered end, M: measurement location)

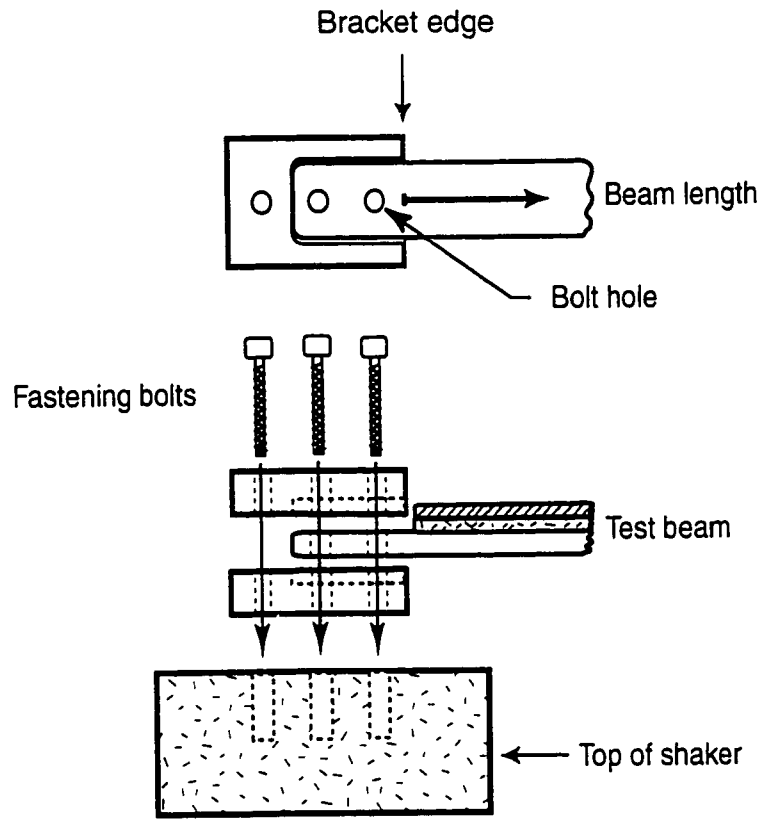

Figure 3.2 The design of the cantilevered end for specimens

mil). Since ISD 112 is pressure-sensitive and self-adhesive, the effect of this lamination on the overall viscoelastic material properties cannot be assessed rigorously. This might introduce uncertainties in interpreting the experimental results.

• **Measurement Details:** In the experiments, two laser vibrometers simultaneously measured the transverse displacement of the base beam $w'_1(x', t)$, and the transverse displacement of the constraining layer $w'_3(x', t)$. For the fully treated beams, the measurement point was at the free end. For the partially treated beams, the measurement points were at the end points of the constraining layers (see Table 3.2). Care was taken to find measuring points that were exactly at the same location but on opposite sides of the test beam.

During the experiments, the acceleration $\frac{\partial^2}{\partial t^2} w'_1(0, t)$ of the cantilevered end was measured as the input excitation. The spectrum analyzer was used to compute the FRFs of the base beam and the constraining layer through $W_b(\omega)=W'_1(L, \omega)/W'_1(0, \omega)$ and $W_c(\omega)=W'_3(L, \omega)/W'_1(0, \omega)$, respectively, where ω is the frequency, and $W'_1(x', \omega)$ and $W'_3(x', \omega)$ are the Fourier spectrum of $w'_1(x', t)$ and $w'_3(x', t)$. The first six modes ranging from 0 to 8000 Hz were measured.

• **Vibrometer Calibration:** To ensure that both vibrometers have identical calibration, transverse vibration of an untreated base beam at the free end was measured simultaneously by the two vibrometers from opposite sides. Comparison of FRFs obtained from both vibrometers and the accelerometer indicates that the difference is less than 0.5% of the transverse vibration.

3.2 Experimental Results

Figure 3.3 shows the magnitude of W_b and W_c for specimen S_{13} (fully treated, 2.04 mm viscoelatic layer) at six different modes. Note that the difference between the magnitude of the FRF for the base beam $|W_b|$ and the magnitude of the FRF for the constraining layer $|W_c|$ becomes more noticeable as the frequency increases from the first mode to the sixth mode. (The measured phases of W_b and W_c are identical over the entire frequency range and are therefore not shown in the figure.) Also, $|W_b|$ is always greater than $|W_c|$. Specimens S_{11} and S_{12}, with thinner viscoelastic layers, have the same vibration behavior.

Figure 3.3 also demonstrates that direct measurements can detect small amounts of thickness deformation that would have been very difficult to detect using indirect techniques. Figures 3.4 and 3.5 show the magnitude of W_b and W_c for specimens S_{23} and S_{33} at six different modes. Recall that these specimens were partially treated with different lengths of damping treatments. The results show that $|W_b|$ is not always greater than $|W_c|$. Instead, $|W_b|$ is greater than $|W_c|$ at odd numbered modes, and smaller at even numbered modes. Other specimens in groups 2 and 3 showed the same behavior.

To quantify the thickness deformation of all specimens on an equal basis, a relative thickness deformation (RTD) index is defined as $|(W_b - W_c)/ W_b|$. Figure 3.6 shows RTD versus frequency for all specimens. The markers denote the experimental RTD at resonant frequencies. There are several note worthy features in Figure 3.6. First, RTD increases as thickness of the viscoelastic layer increases. Second, partially treated specimens with shorter damping treatments have greater RTD. Third, for group 1 (i.e., fully treated specimens), frequency seems to play an influential role in the thickness deformation. RTD increases as frequency increases, implying that thickness deformation becomes more noticeable at higher frequency ranges. For partially treated specimens in groups 2 and 3, however, modes instead of frequencies, seem to dominate RTD. For example, RTD at mode 3 (near 1250 Hz) is greater than that at mode 4 (near

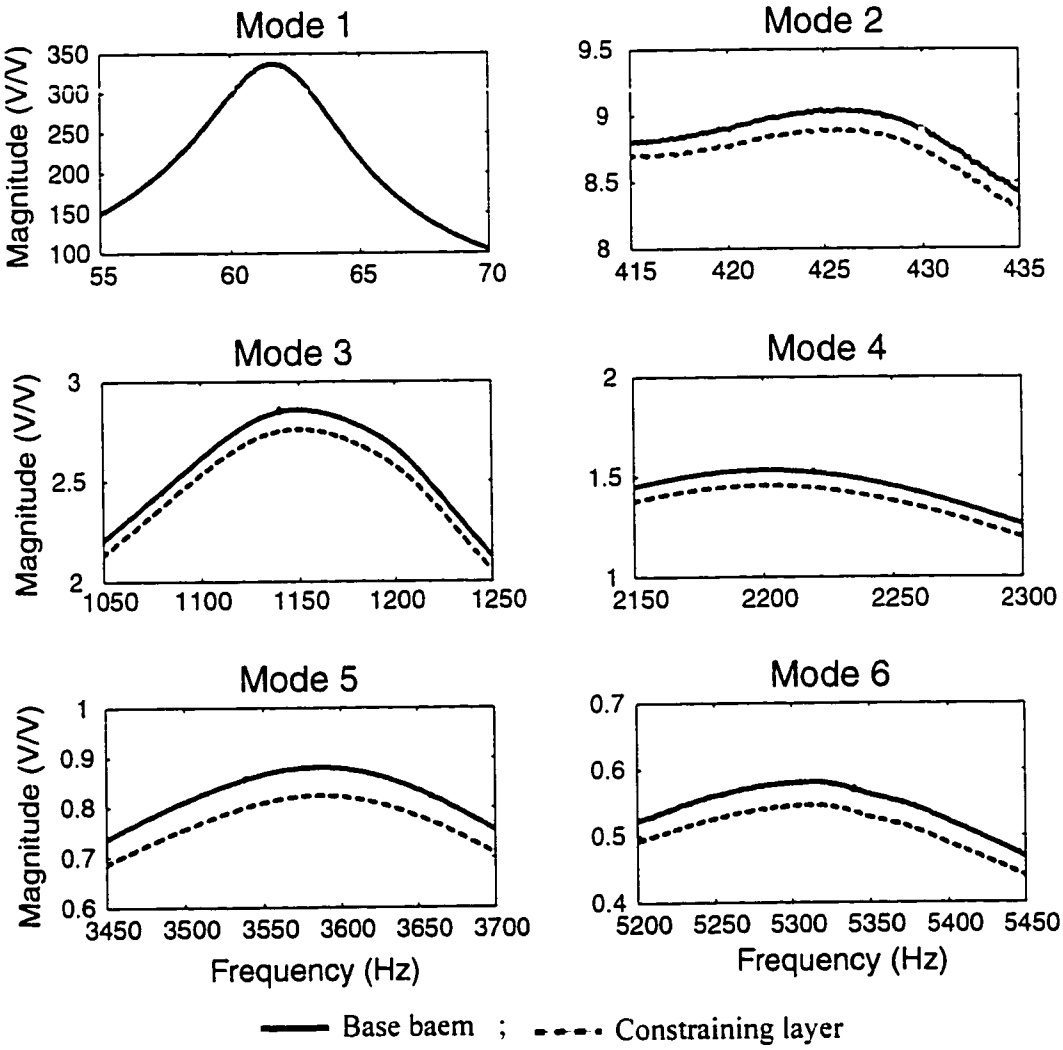

Figure 3.3 FRFs of specimen S_{13}

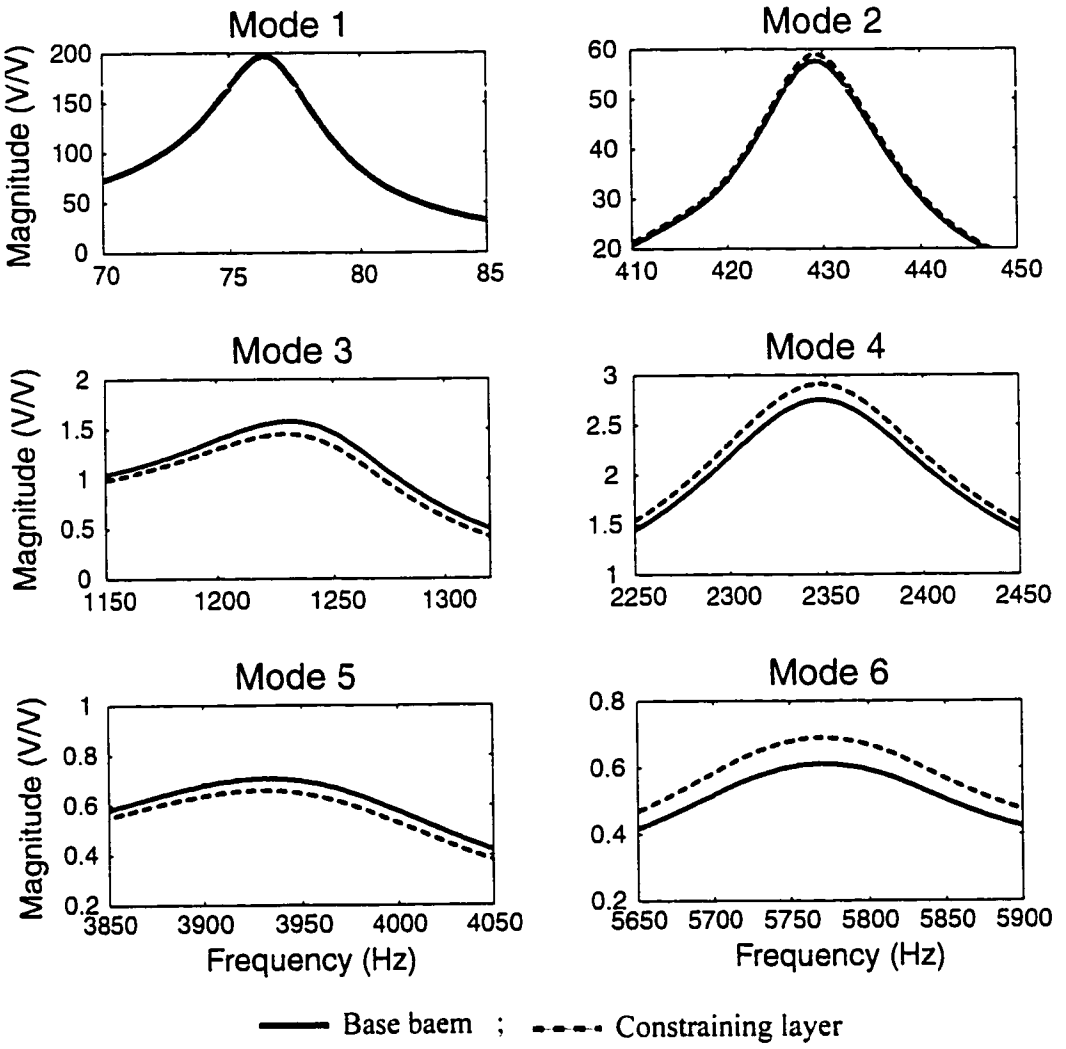

Figure 3.4 FRFs of specimen S_{23}

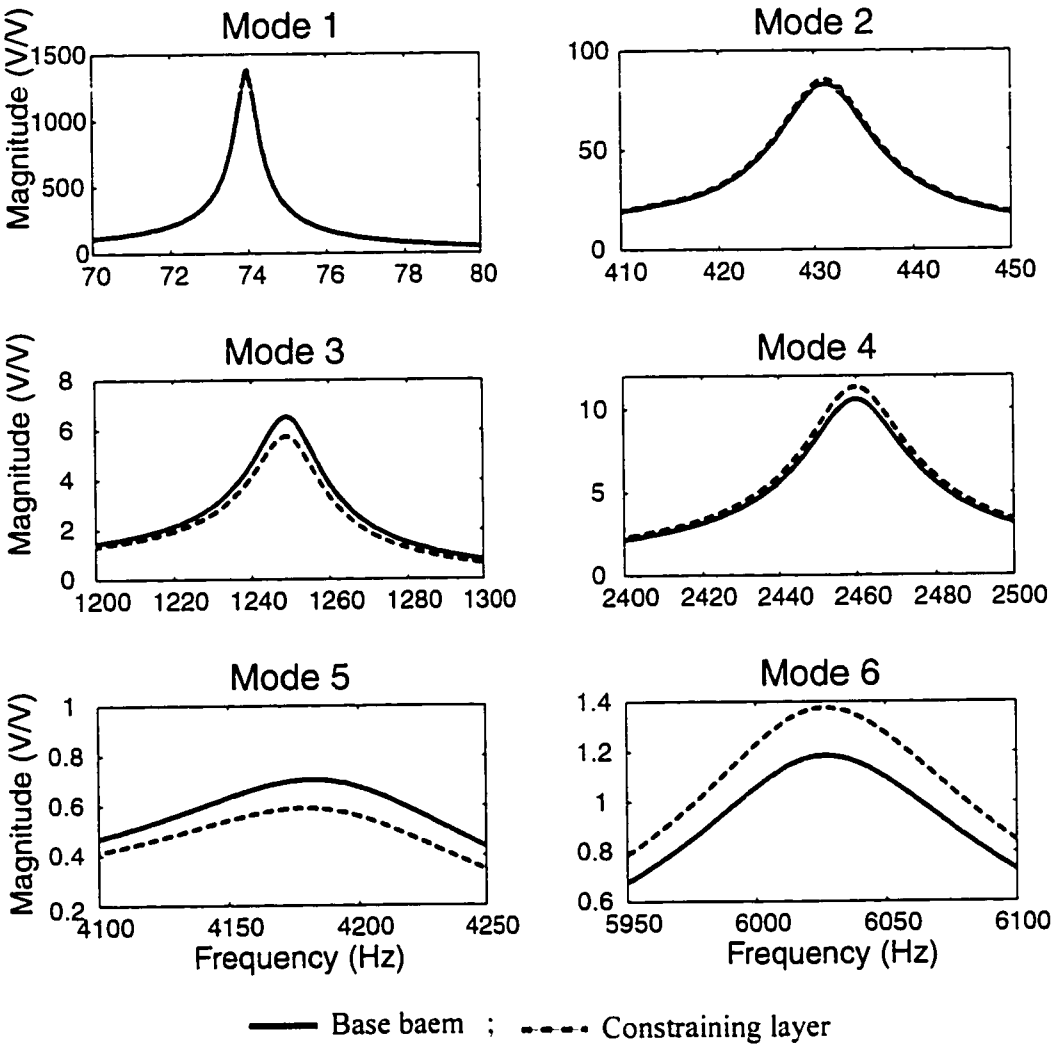

Figure 3.5 FRFs of specimen S_{33}

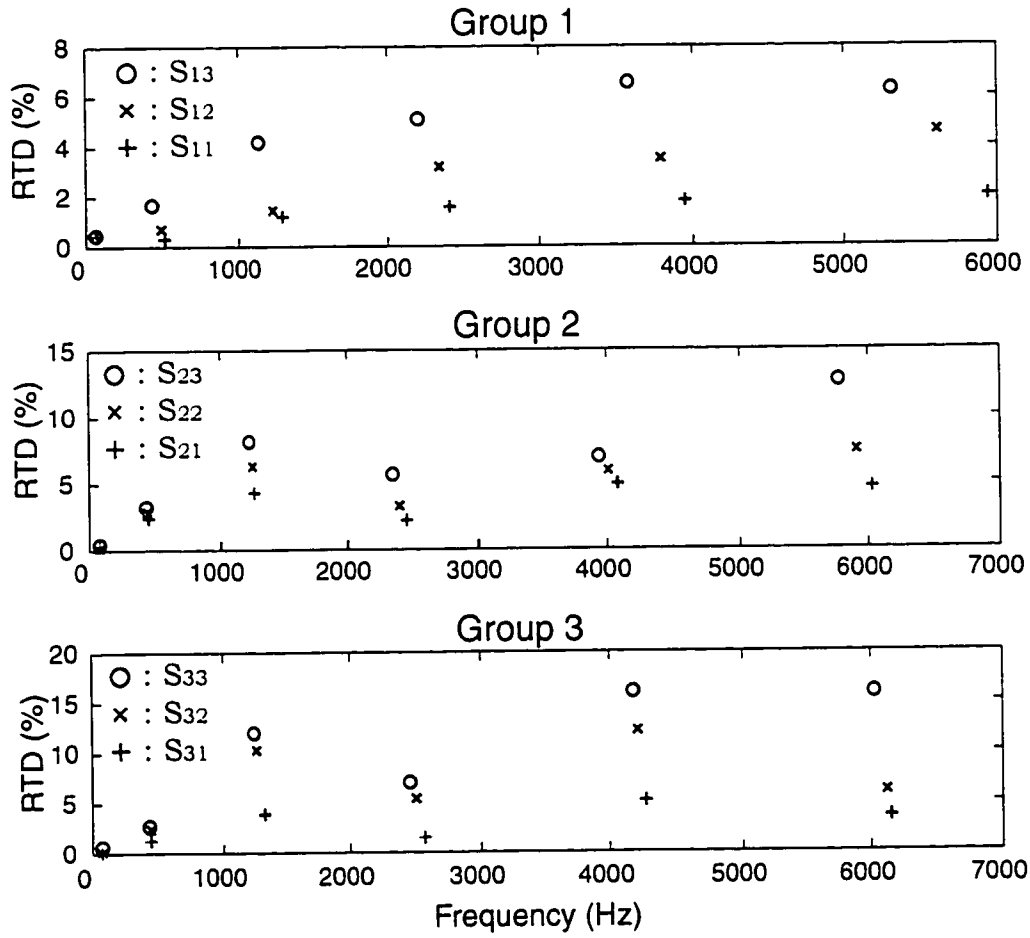

Figure 3.6 RTD index for all specimens

2450 Hz) for all specimens in these two groups. Finally, vibrometer calibration ensures that our direct measurement technique can detect thickness deformation with RTD as low as 0.5%.

3.3 Theoretical Analysis

Our theoretical analysis can be divided into three parts. The first part is to normalize and rewrite the equations of motion derived by Miles and Reinhall [8] into a state-space representation. Then the method of distributed transfer functions [16] is used to compute the FRFs predicted from the TD model.

The second part is to compare the FRFs predicted from the TD model with those predicted from the MMM model. Comparison with the original Mead-Markus model is not possible, because the Mead-Markus model cannot describe the boundary conditions at the cantilevered end (Trompette et al., 1978). The third part of this section compares the theoretical predictions from both models with the experimentally measured FRFs. Modeling partially treated beams substantially increases the order of the TD model. Therefore, for the purpose of demonstrating the concept, the theoretical analysis will only focus on fully treated beams.

3.3.1 Solving Equations of Motion for the TD Model

The variable fields used in the TD model are shown in Figure 1.2. Let x' and t be the space and time variables. In addition, the transverse and longitudinal displacements of the j-th layers are $w_j'(x', t)$ and $u_j'(x', t)$, respectively. Furthermore, $\bar{w}_j'(x', s')$ and $\bar{u}_j'(x', s')$ are Laplace transforms of $w_j'(x', t)$ and $u_j'(x', t)$, where s' is the Laplace transform parameter. The subscripts $j = 1, 2, 3$ refer to the base beam, the viscoelastic layer, and the constraining layer, respectively. For the j-th layer, the thickness is H_j, density is ρ_j, Poisson's ratio is ν_j, complex shear modulus G_j^*, and complex Young's modulus E_j^*. Moreover, $G_j^* = G_j(1+i\eta_j)$, where G_j is the storage modulus and η_j is the loss factor. Similarly, $E_j^* = E_j(1+i\eta_j)$, where $E_j = 2(1+\nu_j)G_j$. All three layers have rectangular cross sections with the same length L and width b.

To derive the equation of motion, the first step is to define a dimensionless space variable x and a dimensionless Laplace transform variable s as

$$x = \frac{x'}{L}, \quad s = s' \cdot \sqrt{\frac{L' V_t}{I_t E_t}} \tag{3.1}$$

Then the variable fields in the TD model are non-dimensionalized in the Laplace transform through

$$w_1(x,s) = \frac{\overline{w}'_1(x',s')}{H_1}, \quad w_3(x,s) = \frac{\overline{w}'_3(x',s')}{H_1} \tag{3.2}$$

$$u_1(x,s) = \overline{u}'_1(x',s') \cdot \frac{L}{H_1}\sqrt{\frac{A_1}{I_1}}, \quad u_3(x,s) = \overline{u}'_3(x',s') \cdot \frac{L}{H_1}\sqrt{\frac{A_1}{I_1}} \tag{3.3}$$

With the dimensionless variables w_1, w_3, u_1, and u_3, the equations of motion derived by Miles and Reinhall (1986) can be normalized and expressed in the following matrix form

$$\left\{ \begin{bmatrix} s^2 + C_1 + \frac{d^4}{dx^4} & -C_1 & 0 & 0 \\ -C_1 & C_1 + C_3 s^2 + C_2 \frac{d^4}{dx^4} & 0 & 0 \\ 0 & 0 & C_4 s^2 - \frac{d^2}{dx^2} & 0 \\ 0 & 0 & 0 & C_1 C_4 s^2 - C_5 \frac{d^2}{dx^2} \end{bmatrix} \right.$$

$$\left. + \xi \begin{bmatrix} -\frac{d^2}{dx^2} & -B_{12}\frac{d^2}{dx^2} & -B_{13}\frac{d}{dx} & B_{13}\frac{d}{dx} \\ -B_{12}\frac{d^2}{dx^2} & -B_{22}\frac{d^2}{dx^2} & -B_{23}\frac{d}{dx} & B_{23}\frac{d}{dx} \\ B_{13}\frac{d}{dx} & B_{23}\frac{d}{dx} & B_{33} & -B_{33} \\ -B_{13}\frac{d}{dx} & -B_{23}\frac{d}{dx} & -B_{33} & B_{33} \end{bmatrix} \right\} \begin{Bmatrix} w_1 \\ w_3 \\ u_1 \\ u_3 \end{Bmatrix} = \begin{Bmatrix} 0 \\ 0 \\ 0 \\ 0 \end{Bmatrix} \tag{3.4}$$

The coefficients in (3.4) are

$$C_1 = \frac{L^4 M_2}{I_1 E_1},\quad C_2 = \frac{I_3 E_3}{I_1 E_1},\quad C_3 = \frac{V_3}{V_1},\quad C_4 = \frac{I_1}{L^2 A_1},\quad C_5 = \frac{A_3 E_3}{A_1 E_1} \tag{3.5}$$

$$B_{12} = \frac{T_2}{T_1},\quad B_{23} = \frac{T_3}{T_1},\quad B_{33} = \frac{I_3}{A_3 H_2^2 I_1},\quad B_{11} = \frac{I_1 M_1}{\sqrt{I_1 A_1 H_2 I_1}},\quad B_{13} = \frac{I_1 M_3}{\sqrt{I_1 A_1 H_2 I_1}} \tag{3.6}$$

$$\xi = \frac{bG_2^* L^2 H_2 T_1}{I_1 E_1} \tag{3.7}$$

where

$$A_j = b \cdot H_j,\quad I_j = \frac{bH_j^3}{12},\quad j=1,2,3 \tag{3.8}$$

$$V_1 = \rho_1 A_1 + \frac{\rho_2 A_2}{2},\quad V_3 = \rho_3 A_3 + \frac{\rho_2 A_2}{2}$$

and

(3.9)

$$T_1 = \frac{1}{2}\left(\frac{2}{3} + \frac{H_1}{H_2} + \frac{H_1^2}{2H_2^2}\right),\quad T_3 = \frac{1}{2}\left(\frac{2}{3} + \frac{H_3}{H_2} + \frac{H_3^2}{2H_2^2}\right),\quad T_2 = \frac{1}{2}\left(\frac{1}{3} + \frac{H_1 + H_3}{2H_2} + \frac{H_1 H_3}{2H_2^2}\right) \tag{3.10}$$

$$M_1 = \frac{1}{2}\left(1 + \frac{H_1}{H_2}\right),\quad M_3 = \frac{1}{2}\left(1 + \frac{H_3}{H_2}\right),\quad M_2 = \frac{E_2^* A_2}{H_2^2} \tag{3.11}$$

To rewrite (3.4) into a state-space form, define a state vector

$$y(x,s) = \left\{ w_1, \frac{dw_1}{dx}, \frac{d^2 w_1}{dx^2}, \frac{d^3 w_1}{dx^3}, w_3, \frac{dw_3}{dx}, \frac{d^2 w_3}{dx^2}, \frac{d^3 w_3}{dx^3}, u_1, \frac{du_1}{dx}, u_3, \frac{du_3}{dx} \right\}^T \tag{3.12}$$

Then equations of motion (3.4) can be rewritten as

$$\frac{dy(x,s)}{dx} = F(s) \cdot y(x,s) \tag{3.13}$$

where

$$F(s) =$$

$$\begin{bmatrix}
0 & 1 & 0 & 0 & 0 & 0 & 0 & 0 & 0 & 0 & 0 & 0 \\
0 & 0 & 1 & 0 & 0 & 0 & 0 & 0 & 0 & 0 & 0 & 0 \\
0 & 0 & 0 & 1 & 0 & 0 & 0 & 0 & 0 & 0 & 0 & 0 \\
\dfrac{-C_1 - s^2}{E_1^n} & 0 & \dfrac{\xi}{E_1^n} & 0 & \dfrac{C_1}{E_1^n} & 0 & \dfrac{\xi B_{12}}{E_3^n} & 0 & 0 & \dfrac{\xi B_{13}}{E_1^n} & 0 & \dfrac{-\xi B_{13}}{E_1^n} \\
0 & 0 & 0 & 0 & 0 & 1 & 0 & 0 & 0 & 0 & 0 & 0 \\
0 & 0 & 0 & 0 & 0 & 0 & 1 & 0 & 0 & 0 & 0 & 0 \\
0 & 0 & 0 & 0 & 0 & 0 & 0 & 1 & 0 & 0 & 0 & 0 \\
\dfrac{C_1}{C_2 E_1^n} & 0 & \dfrac{\xi B_{12}}{C_2 E_3^n} & 0 & \dfrac{-C_1 - C_3 s^2}{C_2 E_3^n} & 0 & \dfrac{\xi B_{23}}{C_2 E_3^n} & 0 & 0 & \dfrac{\xi B_{23}}{C_2 E_3^n} & 0 & \dfrac{-\xi B_{23}}{C_2 E_3^n} \\
0 & 0 & 0 & 0 & 0 & 0 & 0 & 0 & 1 & 0 & 0 & 0 \\
0 & \dfrac{\xi B_{13}}{E_1^n} & 0 & 0 & 0 & \dfrac{\xi B_{23}}{E_1^n} & 0 & 0 & \dfrac{-C_4 s^2 + \xi B_{33}}{E_1^n} & 0 & \dfrac{-\xi B_{33}}{E_1^n} & 0 \\
0 & 0 & 0 & 0 & 0 & 0 & 0 & 0 & 0 & 0 & 0 & 1 \\
0 & \dfrac{-\xi B_{13}}{C_3 E_1^n} & 0 & 0 & 0 & \dfrac{-\xi B_{23}}{C_3 E_1^n} & 0 & 0 & \dfrac{-\xi B_{33}}{C_3 E_1^n} & 0 & \dfrac{C_3 C_4 s^2 - \xi B_{33}}{C_3 E_1^n} & 0
\end{bmatrix} \tag{3.14}$$

and

$$E_1^n = (1 + i \cdot \eta_1), \quad E_3^n = (1 + i \cdot \eta_3)$$

Consider the boundary conditions shown in Figure 2.6 where we let the both ends of constraining layer free and cantilevered the base beam on the shaker. In addition, let $P(s)$ be the normalized displacement excitation from the shaker. We also normalized the dimension and made the length of base beam become 1. Therefore, we obtained the normalized boundary conditions in the state space form as:

$$M(s)y(0,s) + N(s)y(1,s) = g(s) \tag{3.15}$$

where

$$g(s) = \{P(s),0,0,0,0,0,0,0,0,0,0,0\}^T \tag{3.16}$$

and

$$M(s)=\begin{bmatrix}
1 & 0 & 0 & 0 & 0 & 0 & 0 & 0 & 0 & 0 & 0 & 0 \\
0 & 1 & 0 & 0 & 0 & 0 & 0 & 0 & 0 & 0 & 0 & 0 \\
0 & \frac{-K_3T_2}{E_3^*} & 0 & 0 & 0 & \frac{-K_3T_3}{E_3^*} & 0 & 1 & \frac{-K_3B_{23}T_1}{E_3^*} & 0 & \frac{K_3B_{23}T_1}{E_3^*} & 0 \\
0 & 0 & 0 & 0 & 0 & 0 & 1 & 0 & 0 & 0 & 0 & 0 \\
0 & 0 & 0 & 0 & 0 & 0 & 0 & 0 & 1 & 0 & 0 & 0 \\
0 & 0 & 0 & 0 & 0 & 0 & 0 & 0 & 0 & 0 & 0 & 1 \\
0 & 0 & 0 & 0 & 0 & 0 & 0 & 0 & 0 & 0 & 0 & 0 \\
0 & 0 & 0 & 0 & 0 & 0 & 0 & 0 & 0 & 0 & 0 & 0 \\
0 & 0 & 0 & 0 & 0 & 0 & 0 & 0 & 0 & 0 & 0 & 0 \\
0 & 0 & 0 & 0 & 0 & 0 & 0 & 0 & 0 & 0 & 0 & 0 \\
0 & 0 & 0 & 0 & 0 & 0 & 0 & 0 & 0 & 0 & 0 & 0
\end{bmatrix} \tag{3.17}$$

$$N(s)=\begin{bmatrix}
0 & 0 & 0 & 0 & 0 & 0 & 0 & 0 & 0 & 0 & 0 & 0 \\
0 & 0 & 0 & 0 & 0 & 0 & 0 & 0 & 0 & 0 & 0 & 0 \\
0 & 0 & 0 & 0 & 0 & 0 & 0 & 0 & 0 & 0 & 0 & 0 \\
0 & 0 & 0 & 0 & 0 & 0 & 0 & 0 & 0 & 0 & 0 & 0 \\
0 & 0 & 0 & 0 & 0 & 0 & 0 & 0 & 0 & 0 & 0 & 0 \\
0 & 0 & 0 & 0 & 0 & 0 & 0 & 0 & 0 & 0 & 0 & 0 \\
0 & \frac{-K_1T_1}{E_1^*} & 0 & 1 & 0 & \frac{-K_1T_2}{E_1^*} & 0 & 0 & \frac{-K_1B_{13}T_1}{E_1^*} & 0 & \frac{K_1B_{13}T_1}{E_1^*} & 0 \\
0 & 0 & 1 & 0 & 0 & 0 & 0 & 0 & 0 & 0 & 0 & 0 \\
0 & \frac{-K_3T_2}{E_3^*} & 0 & 0 & 0 & \frac{-K_3T_3}{E_3^*} & 0 & 1 & \frac{-K_3B_{23}T_1}{E_3^*} & 0 & \frac{K_3B_{23}T_1}{E_3^*} & 0 \\
0 & 0 & 0 & 0 & 0 & 0 & 1 & 0 & 0 & 0 & 0 & 0 \\
0 & 0 & 0 & 0 & 0 & 0 & 0 & 0 & 0 & 1 & 0 & 0 \\
0 & 0 & 0 & 0 & 0 & 0 & 0 & 0 & 0 & 0 & 0 & 1
\end{bmatrix} \tag{3.18}$$

In addition, K_1 and K_3 in (3.17) and (3.18) are

$$K_1=\frac{bG_2^*L^2H_2}{I_1E_1},\quad K_3=\frac{bG_2^*L^2H_2}{I_3E_3} \tag{3.19}$$

According to Yang and Tan (1992), the solution of (3.13) with boundary conditions (3.15) is

$$y(x,s) = e^{F(s)x} \cdot A^{-1}(s) \cdot g(s) \tag{3.20}$$

where

$$A(s) = M(s) + N(s) \cdot e^{F(s)} \tag{3.21}$$

In computing the FRFs of the base beam and the constraining layer, $P(s)$ was set to 1 and the transverse displacements w_1 and w_3 are the first and the fifth element of $y(x, s)$; see (3.12). Similarly, the matrix equations of motion of the MMM model derived by Shen (1994) can be normalized and solved to obtain the transverse displacement of the base beam.

3.3.2 Theoretical Results

The purpose of the numerical simulations was to predict the FRFs of the fully treated specimens in group 1 through the use of the TD and the MMM models. In the simulations, the storage modulus and loss factor of the viscoelastic material were obtained from the experimental data presented by Soovere and Drake (1985). The Poisson ratio of the viscoelastic layer was assumed to be a constant 0.45. The dimensions and material properties of the base beam and the constraining layer are specified in Tables 3.1 and 3.2.

Figure 3.7 shows the predicted FRF of specimen S_{13} using the TD model. The FRFs for the base beam and the constraining layer agree well in the low frequency entire frequency range (not observable from in the figures). Also, the constraining layer has a larger displacement than the base beam.

Figure 3.8 compares the FRFs predicted from the MMM and the TD models for specimen S_{11} and S_{13} (i.e., "thin" versus "thick" viscoelastic layer). The FRFs predicted from the MMM and the TD models agree well in the low frequency range, but diverge significantly in the high frequency range (especially S_{13}). The experimental results discussed in Section 3.2 and shown in Figure 3.3 are plotted again in Figure 3.8 for comparison. In general, t he TD model gives better prediction of

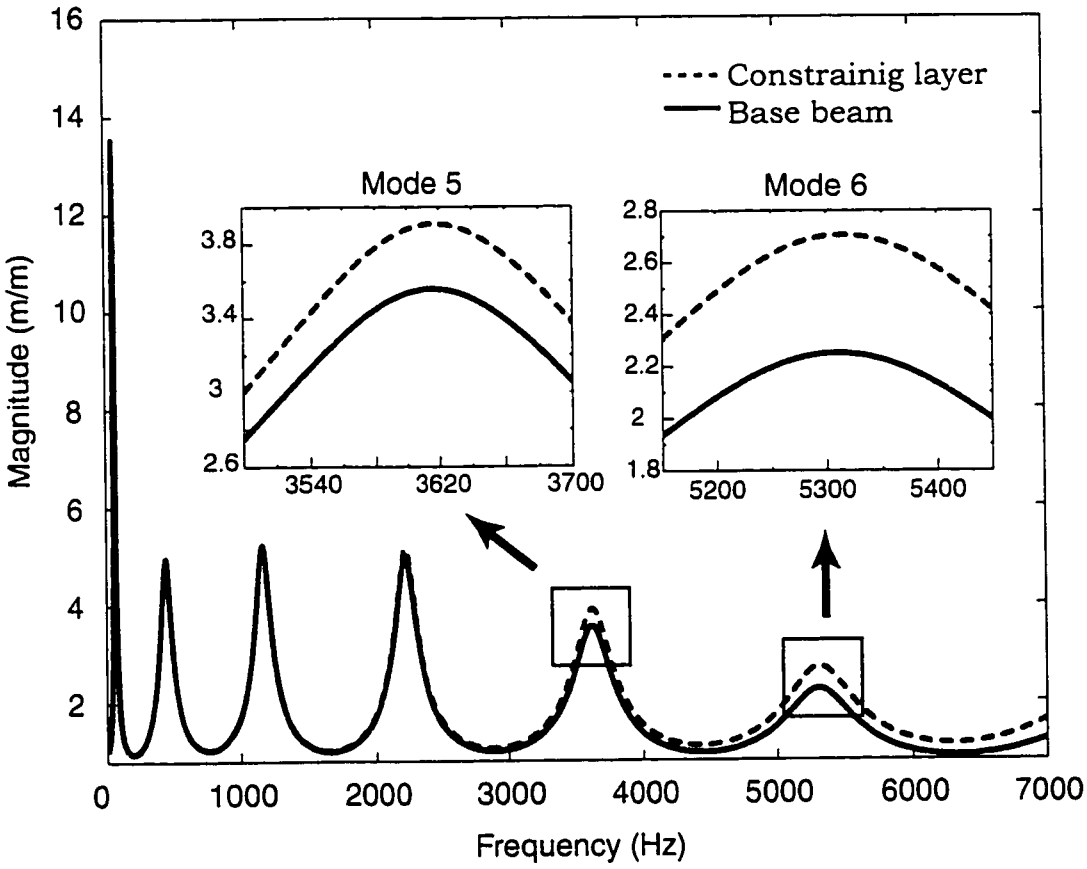

Figure 3.7 Theoretical FRFs for specimen S_{13} based on the TD model

resonant frequencies when thickness deformation is present. Nevertheless, both the TD and the MMM models do not predict the resonance amplitude with high accuracy. This discrepancy is likely a result of the fact that actual properties of viscoelastic materials can often deviate substantially from published values. To evaluate this, a sensitivity analysis was done by varying the Poisson's ratio from 0.35 to 0.49, and varying the complex shear modulus G_2^* from 50% to 150% of the published values. The analysis show that changes of to the Poisson ratio does not change FRFs significantly. However, as shown in Figure 3.9, increasing G_2^* substantially reduces the deviation between experimental and theoretical FRFs.

The validity of the TD model is also demonstrated in Figure 3.10, which compares the theoretical and experimental RTD (Note that the MMM model always results in zero RTD). Figure 3.10 shows that the TD model adequately predicts the experimental RTD. Results from the TD model lie within the bounds from the sensitivity analysis.

3.4 Conclusions

1. A technique that allows direct measurement of thickness deformation in constrained layer treatments is demonstrated in this chapter. This direct measurement technique is feasible and can detect thickness deformation with relative thickness deformation (RTD) as low as 0.5%.
2. For the fully treated CLD beam, the experimental results indicate that RTD increases as frequency increases. For the partially treated CLD beam, the RTD can be significant at lower modes.
3. Experimental results show that RTD increases as thickness of the viscoelastic layer increases. In addition, partial treatments tend to have larger thickness deformation than full treatments.
4. The thickness deformation (TD) model predicts the FRFs better than the modified Mead-Markus (MMM) model when thickness deformation becomes noticeable. The prediction of resonance frequencies from the TD model is

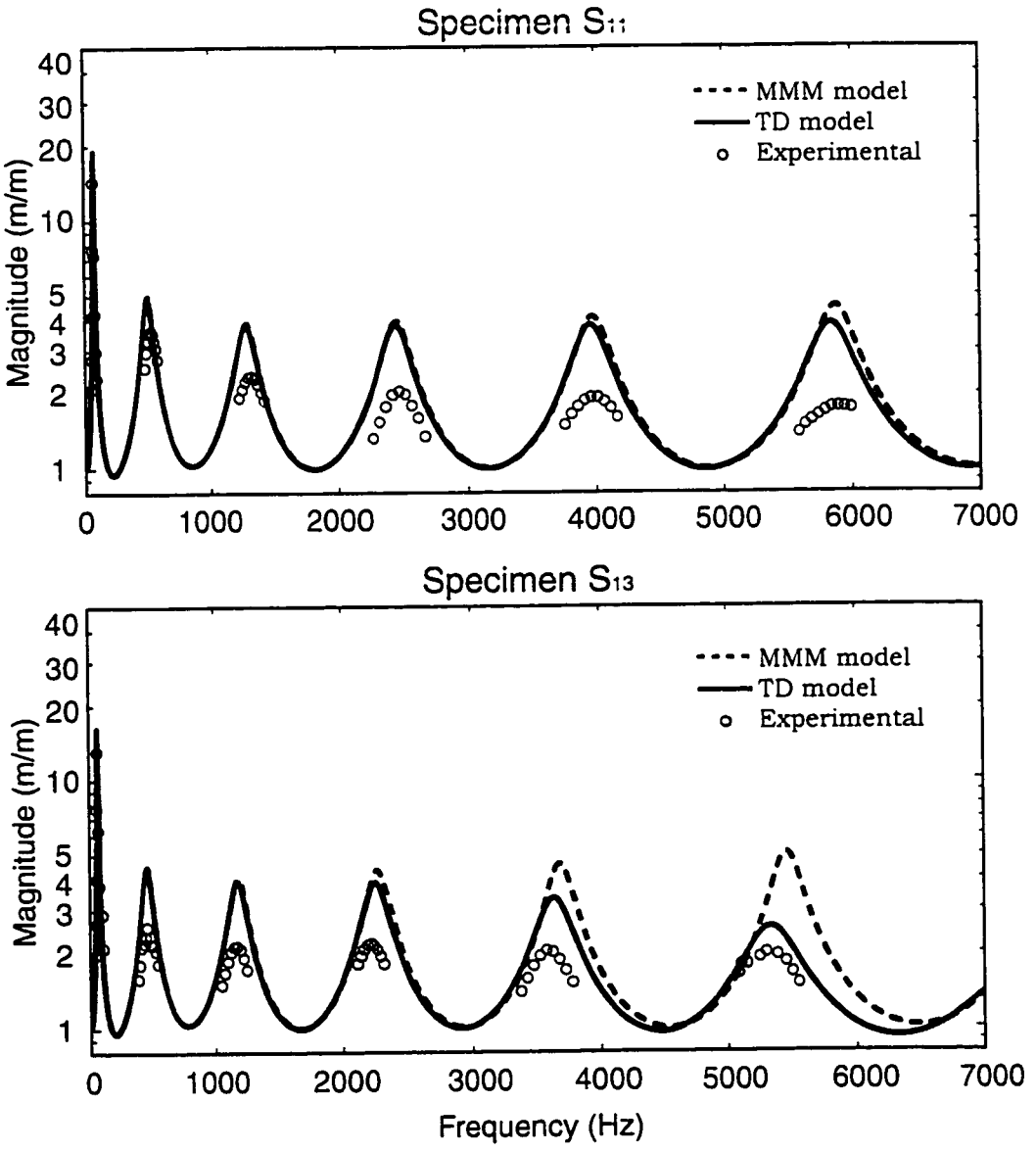

Figure 3.8 FRFs for specimen S_{11} and S_{13} (base beam)

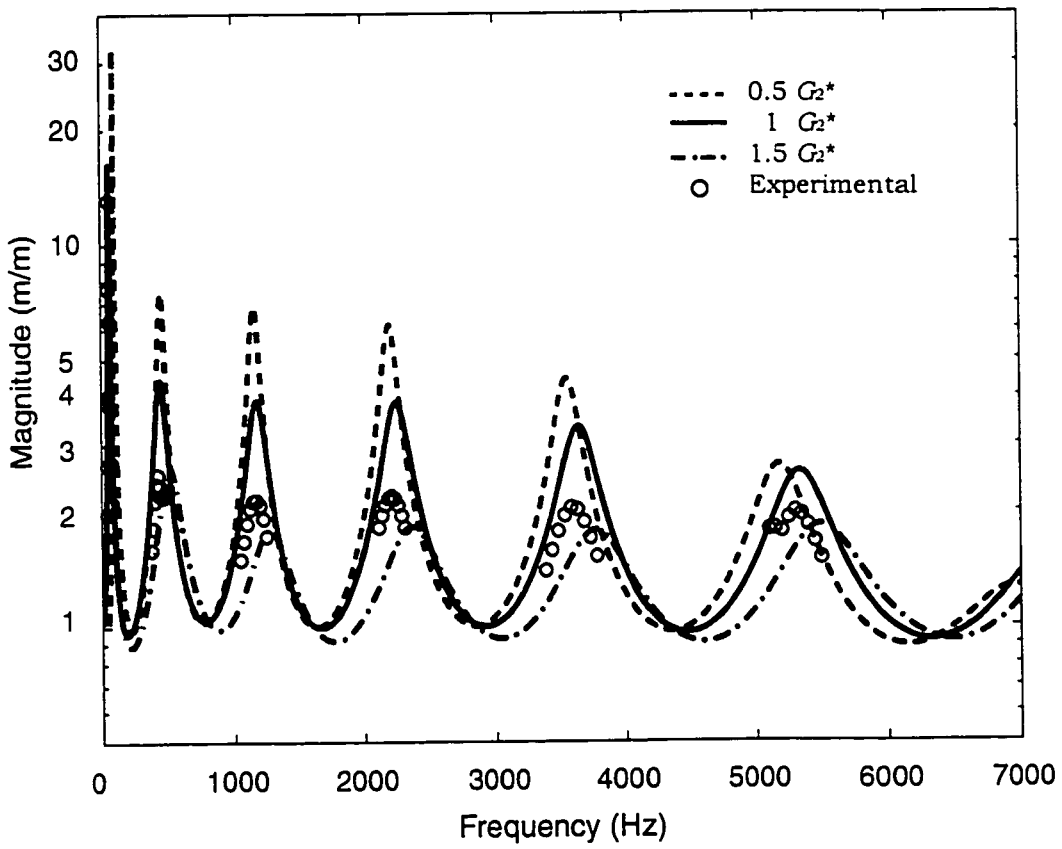

Figure 3.9 Comparison of theoretical (the TD model) and experimental FRFs for specimen S_{13} with 150% and 50% G_2^*

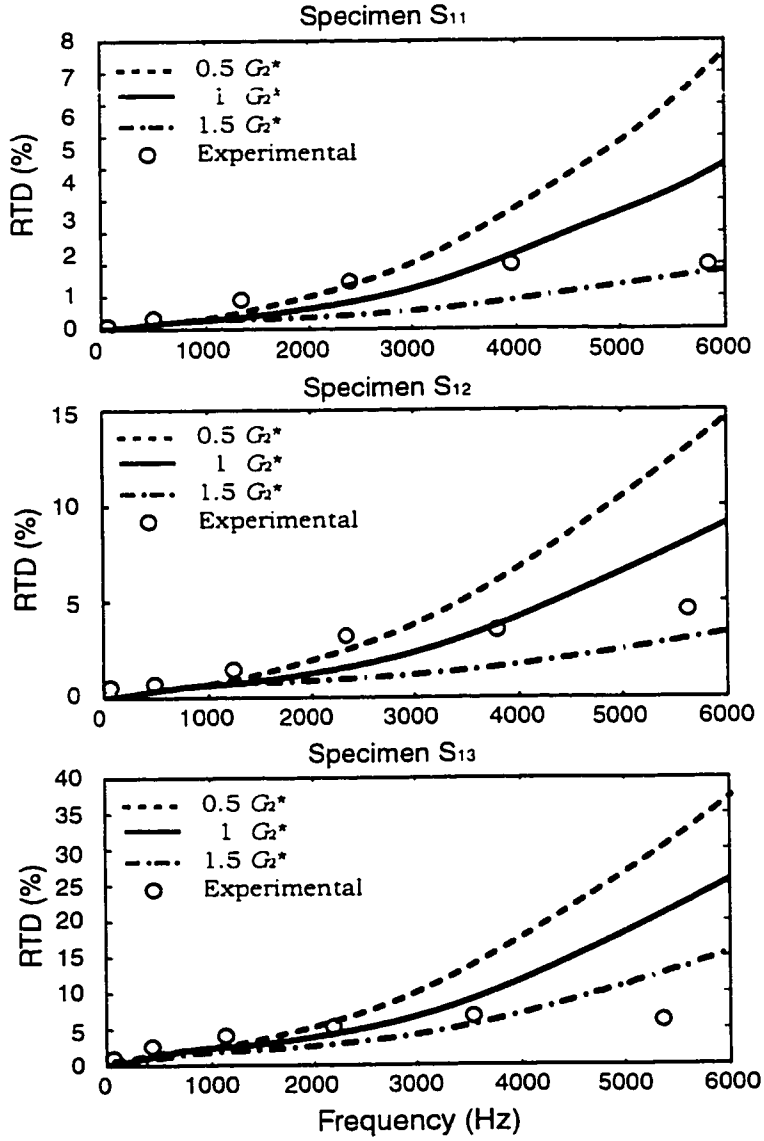

Figure 3.10 Comparison of theoretical (the TD model) and experimental RTD for specimen S_{11}, S_{12} and S_{13} with 150% and 50% G_2^*

accurate. The prediction of resonance amplitudes from the TD model is reasonable, when uncertainties of the properties of the viscoelastic material are taken into account.

Chapter 4

UTILIZATION OF MICROCELLULAR FOAM MATERIALS IN CLD

Microcellular foam materials have been widely used as construction materials, in commercial containers, for sound absorption, and for medical purposes. In this chapter, we evaluate the possibility of using microcellular foam as damping and standoff material in constrained layer damping. In order to achieve this goal, we built a reliable test system based on the ASTM standard and used this system to evaluate dynamic properties such as shear storage modulus and loss factor of microcellular foam. The compression effect on microcellular foam was also investigated.

4.1 Microcellular Foam

The original motivation for developing microcellular foam was to reduce the amount of materials consumed in applications where plastics are used. This foam material can be thought of as a composite material consisting of a polymer matrix surrounding a large number of voids with sizes on the order of 10 μm. In general, these foams are produced in a two-stage process as illustrated in Figure 4.1. First, the polymer is saturated with non-reactive gas in a pressure vessel at a relatively high pressure. After the plastic has become saturated with gas, it is removed from the pressure vessel and then heated up in a liquid bath at the foaming temperature for a length of time to cause bubbles to nucleate and grow. By controlling the manufacturing parameters such as the saturating pressure, saturating time, foaming temperature, and foaming time in this two-stage process, foam with different densities and bubble size can be produced [19].

Based on the property of materials that are full of voids, an assumption that the compressed foam has higher loss factor was investigated. It is assumed that after the foam is compressed, the voids in the foam will be collapsed to become cracks as

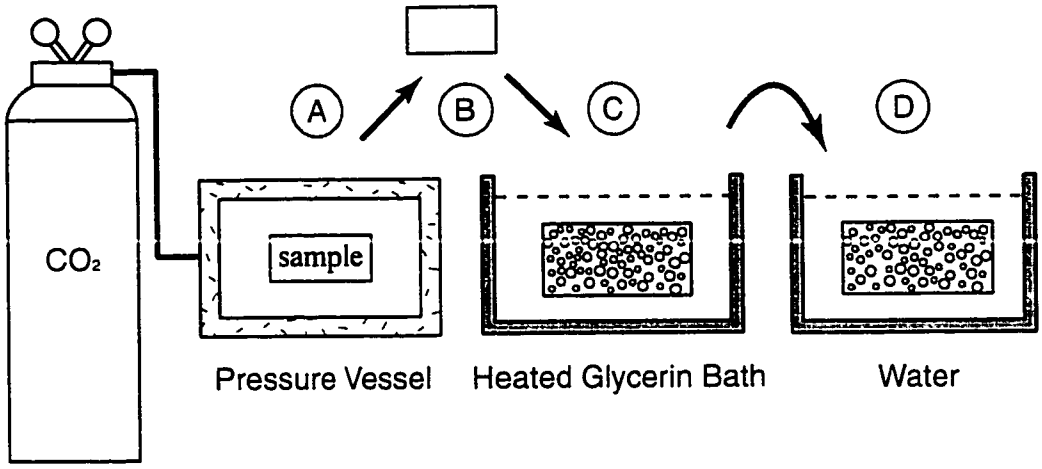

A: Saturating the virgin material sample in a pressure vessel
B: Desorbing the saturated virgin material sample in air
C: Foaming the sample in heated glycerin
D: Cooling down the sample in room temperature water

Figure 4.1 Manufacturing process for PETG microcellular foam

Table 4.1 Manufacturing parameters for foam sample and thier configurations

Foam No.	Virgin Material Thickness (mm)	Manufacturing Parameters				Final Thickness (mm)	Final Density (Kg/m^3)
		Saturating Pressure (psi)	Saturating Time (Hour)	Foaming Temp (°F)	Foaming Time (Sec)		
F_1	0.76	600	48	200	25	1.53	200
F_2	5.08	600	22	255	60	1.7	42
F_3	1.01	600	96	255	60	3.2	45
F_4	0.76	400	48	220	60	2	100
F_5	0.76	500	48	210	30	1.7	150
F_6	0.76	700	48	200	15	1.5	240

illustrated in Figure 4.2. When the compressed foam layer undergoes shear deformation, as in CLD, the sliding of cracks may create an efficient Coulomb constrained layer damper. In our research, we investigated the dynamic properties of the modified polyethylene teraphthalate (PETG) foam with different densities and compression. Table 4.1 shows the manufacturing parameters for our foam specimens and their density.

4.2 Microclellular Foam as Damping Material

We investigated the dynamic properties of PETG foam with different densities. In this section, we first describe the preparation of foam including the manufacturing parameters for our foam and their densities and the manufacturing process to compress the foam. The measurement system is then described and followed by our test results.

4.2.1 Manufacturing Collapsed Microcellular Foam

To manufacture collapsed microcellular foam, the uncompressed PETG foam specimen F_1 was trimmed to 25.4 x 25.4 mm^2 (1"x 1") pieces. Before any specimen was compressed, the thickness of the specimen was measured. The specimen was then placed in a hot-press machine to compress the foam. The compression load, compression time, and compression temperature of the hot-press machine are controllable. After the desired compression processes were completed, the thickness and the area of the specimen were measured. Then the compression thickness ratio (CTR) that is defined as the ratio of thickness of the compressed foam to the thickness of the uncompressed foam was calculated. The smaller the CTR, the thinner the compressed foam.

In this section, we evaluate four factors influencing the thickness of collapsed microcellular foam in the manufacturing process.

Compression load: The compression load was the first factor to be evaluated. Six identical F_1 samples were compressed by using different loads at room

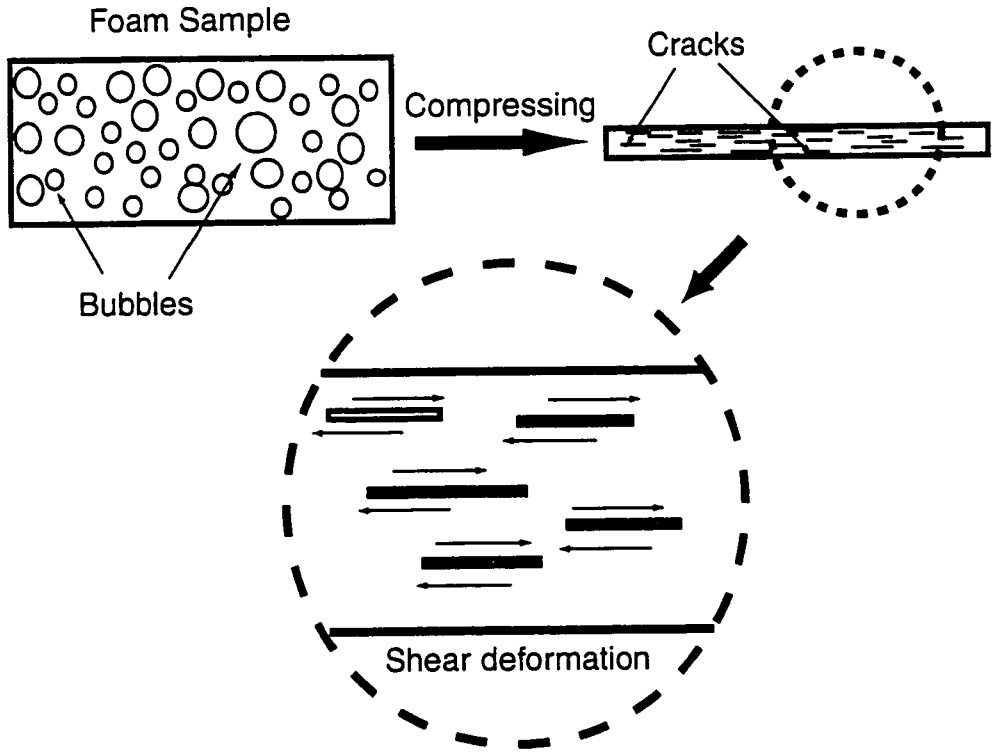

Figure 4.2 The assumptions of compressed foam

temperature (73 °F) for one minute. Note that after the load was released, the compressed foam always bounced back a little after a certain amount of time. The bouncing back behavior of the foam means that some air is still in the foam. The thickness becomes steady after approximately one day. Figure 4.3 shows the relationship between load and steady state CTR. The results show that, with a compression load of 8k lb or more, the steady state CTR are almost the same. The areas for all foams were also measured. The results show that foam cross-sectional area does not change after compression.

In order to verify that when the foam is compressed thinner, more bubbles are actually collapsed, a scanning electron microscope (SEM) was used to inspect the microstructure of the compressed foam. Figure 4.4 shows a comparison of the microstructure of an uncompressed foam and that of a foam compressed under 20k lb load at 73 °F for 3 minutes. Note that most of bubbles in the compressed foam are distorted but not totally collapsed. In order to achieve better compression, we investigated the effect of compression temperature next.

Compression temperature: Five identical F_1 foam samples were compressed under the same load (20k lb) for three minutes at eight different temperatures. The temperature ranges from room temperature (73 °F) to glassy temperature (180 °F - 210 °F). If the compression temperature was higher than room temperature, the specimen was quenched in room temperature water for 1 minute before the thickness and cross sectional area were measured. We observed from our experiments that when the compressing temperature is increased to a certain degree, the foam will not bounce back. Figure 4.5 shows the steady-state CTR against temperature. The results demonstrate that the thinnest compressed foam can be obtained at temperature around 117 °F to 127 °F instead of in the high glassy temperature range. Similar results are also obtained in tests in which the foam was compressed for 20 minutes.

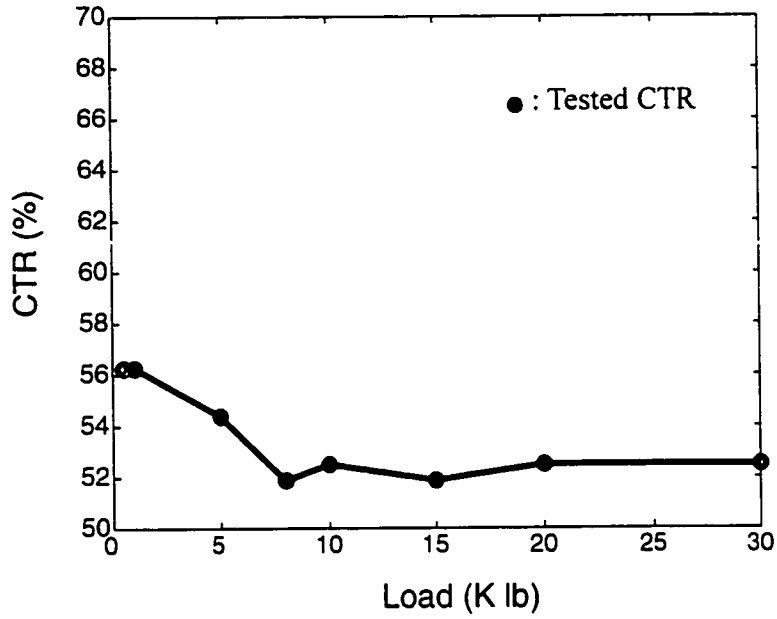

Figure 4.3 Load effect in manufacturing the compressed foam

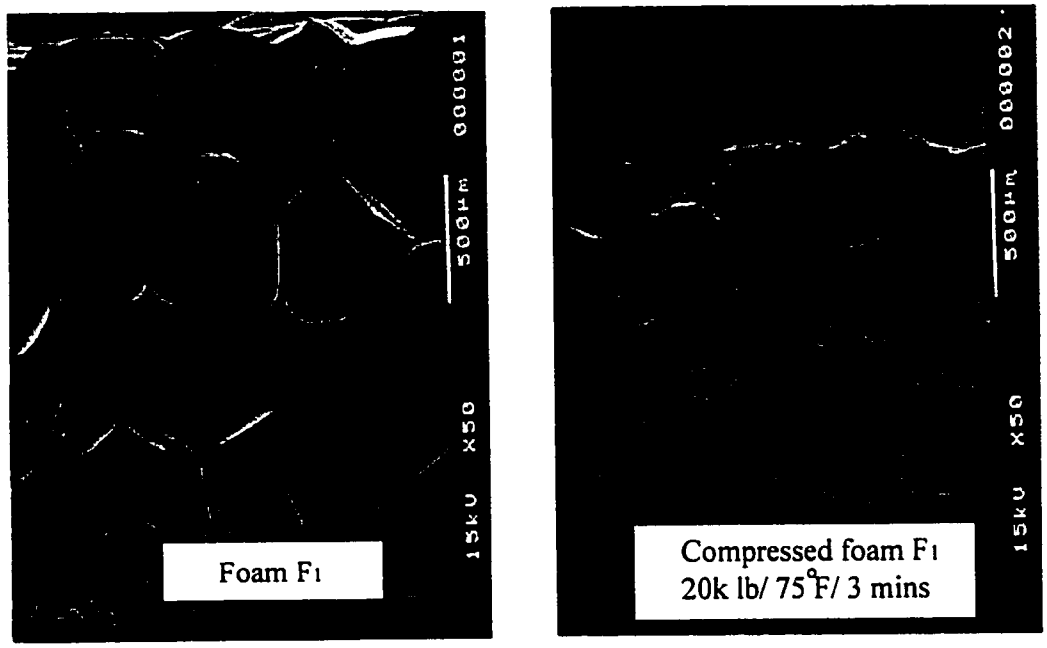

Figure 4.4 Microstructure of the uncompressed and compressed foam (load effect)

Figure 4.6 shows the two microstructure of foams compressed at different temperatures. It shows that the bubbles are not collapsed when compressing the foam at glassy temperature. Compressing the foam at 117 °F actually results in lower CTR. However, still not all of the bubbles are collapsed.

Compression time: In this set of experiments, the compression time effect was evaluated. Four identical F_1 specimens were compressed under the same load (20 k lb) at the same temperature (117 °F) for different lengths of time. The compression time ranges from 3 minutes to 150 minutes. In Figure 4.7, the results show that by increasing the compression time, thinner compressed foams can be obtained. Note that CTR approaches the limit as compression time increases. Figure 4.8 shows that more bubbles are collapsed when the compression time is longer.

Compression cyclic temperature: Instead of compressing the foam at a constant temperature, we evaluated the compression cyclic temperature effect by varying the temperature during compression. Figure 4.9 shows the results obtained without cycle and with one and two cycles. For the one cyclic temperature compression, the foam was first compressed at a temperature of 117 °F for an hour, and then the temperature was increased to 190 °F and the foam was compressed for another hour. Finally, the foam was compressed for a third hour at a decreased temperature of 117 °F.

The results show that when cyclic temperature was used during the compression process, a thinner foam can be obtained. No significant difference in results is observed when the two cycles method is used. Figure 4.10 shows the microstructure of the foam compressed by using the cyclic temperature method. Note that most of the bubbles in the foam were collapsed. This is the optimized manufacture process to compress the foam and collapse the bubbles. In order to investigate if the same optimized compressing process applied to

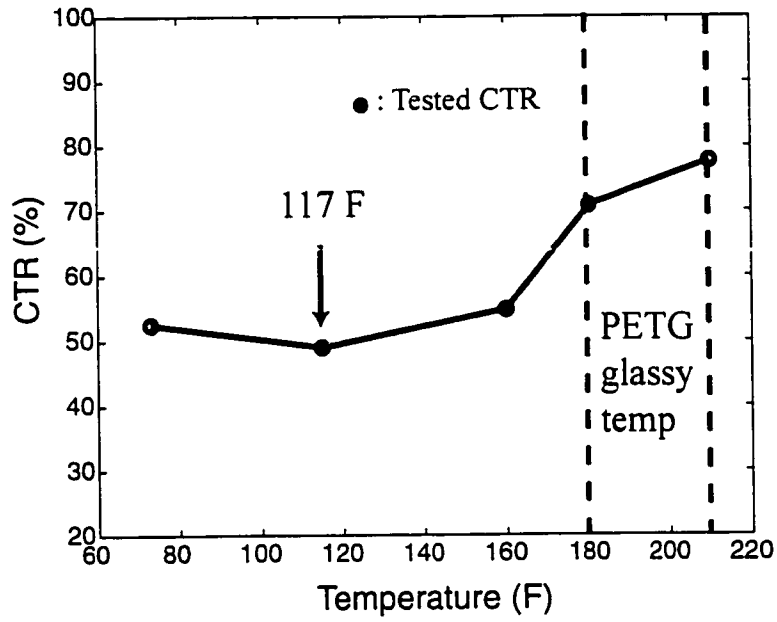

Figure 4.5 Temperature effect in manufacturing the compressed foam

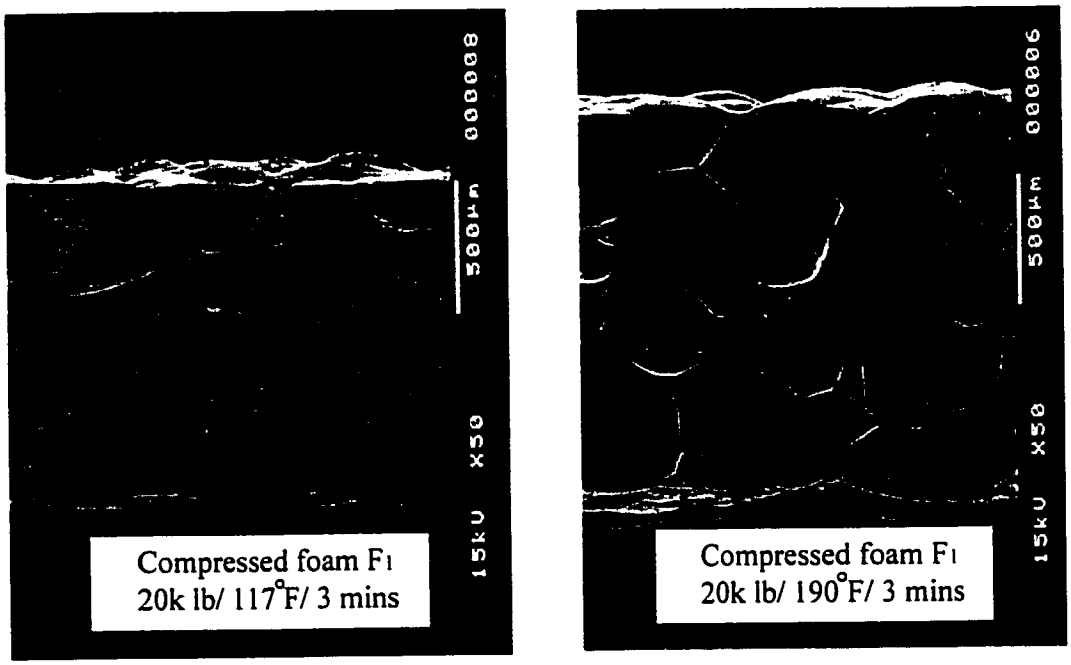

Figure 4.6 Microstructure of the uncompressed and compressed foam (temperature effect)

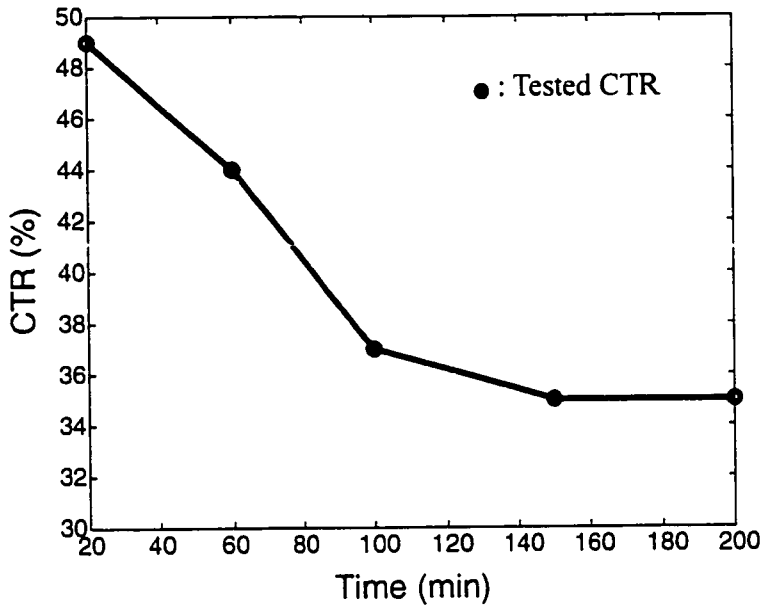

Figure 4.7 Time effect in manufacturing the compressed foam

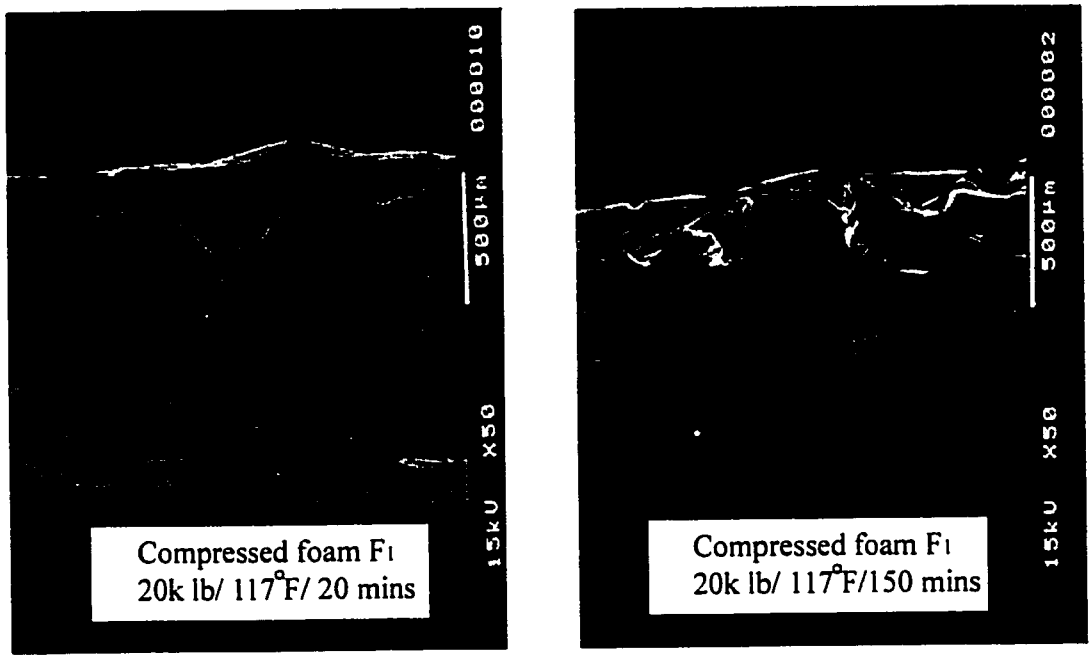

Figure 4.8 Microstructure of the uncompressed and compressed foam (time effect)

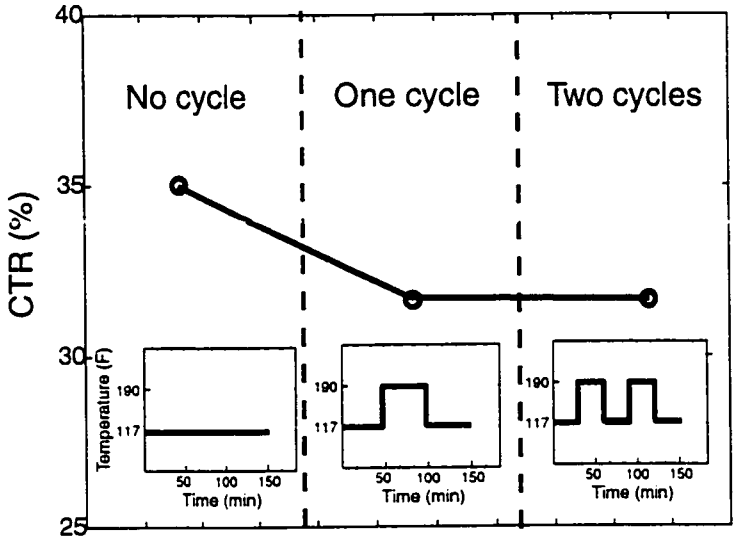

Figure 4.9 Cyclic temperature effect in manufacturing the compressed faom

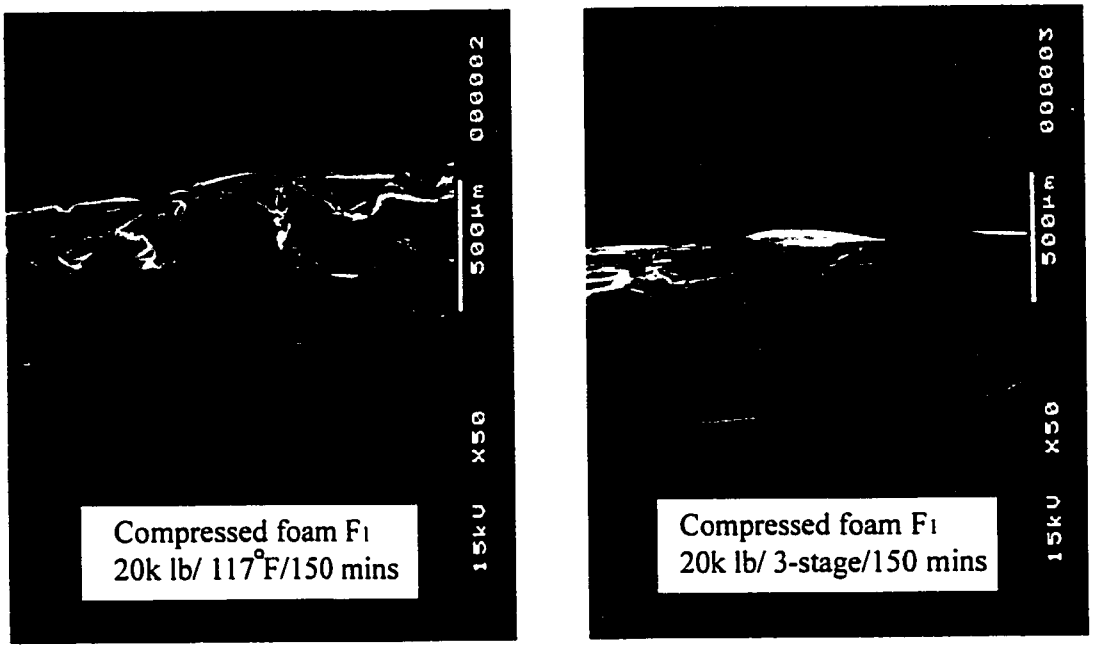

Figure 4.10 Microstructure of the uncompressed and compressed foam (cyclic temperature effect)

other foam, the foam specimen F_2 with different density and bubble size was compressed. Figure 4.11 shows the microstructure of the uncompressed and compressed foam for sample F_1 and F_2 by using cyclic temperature method. Note that after the compression cyclic temperature process, the voids in the foam became fully collapsed. The same method was also applied to compress larger pieces of foam. 101.6x101.6 mm^2 (4"x 4") with satisfying results. Hence, it concluded that the compression cyclic temperature process is the best method to use for collapsing voids.

4.2.2 Test System for Measuring Dynamic Properties of Materials

Our system is based on the ASTM standard with designation: E756-98 [24] which is good for testing the dynamic properties of materials such as metals, enamels, ceramics, rubbers, plastics, reinforces epoxy matrices, and woods. The basic concept behind the method is based on the principle of CLD. When a damping material is bonded between the structure's surface and an elastic constraining layer (whose relative stiffness is greater than that of the damping material), vibratory energy can be dissipated through cyclic shear deformation of the damping materials. The dynamic complex shear modulus and loss factor of the damping material can be calculated from the natural frequencies and the corresponding modal loss factor of the CLD beam by using the principle developed by Ross, Ungar, and Kerwin [3].

Our test specimen was assembled by sandwiching a damping layer into two identical base beams as shown in Figure 4.12. The base beams were made of aluminum and were integrally machined with a root. The dimensions and configurations of the beam are shown in Table 4.2. A spacer with same thickness as the damping material being tested was made to fit into the root section. The Loctite 401 cyanoacrylatester with high shear strength was applied as the adhesive between the damping layer and the base beam. Since the thickness of the adhesive is very small (around 0.005 mm), the damping effect from the adhesive can be ignored. In order to ensure that the two base beams are identical, their FRFs are carefully

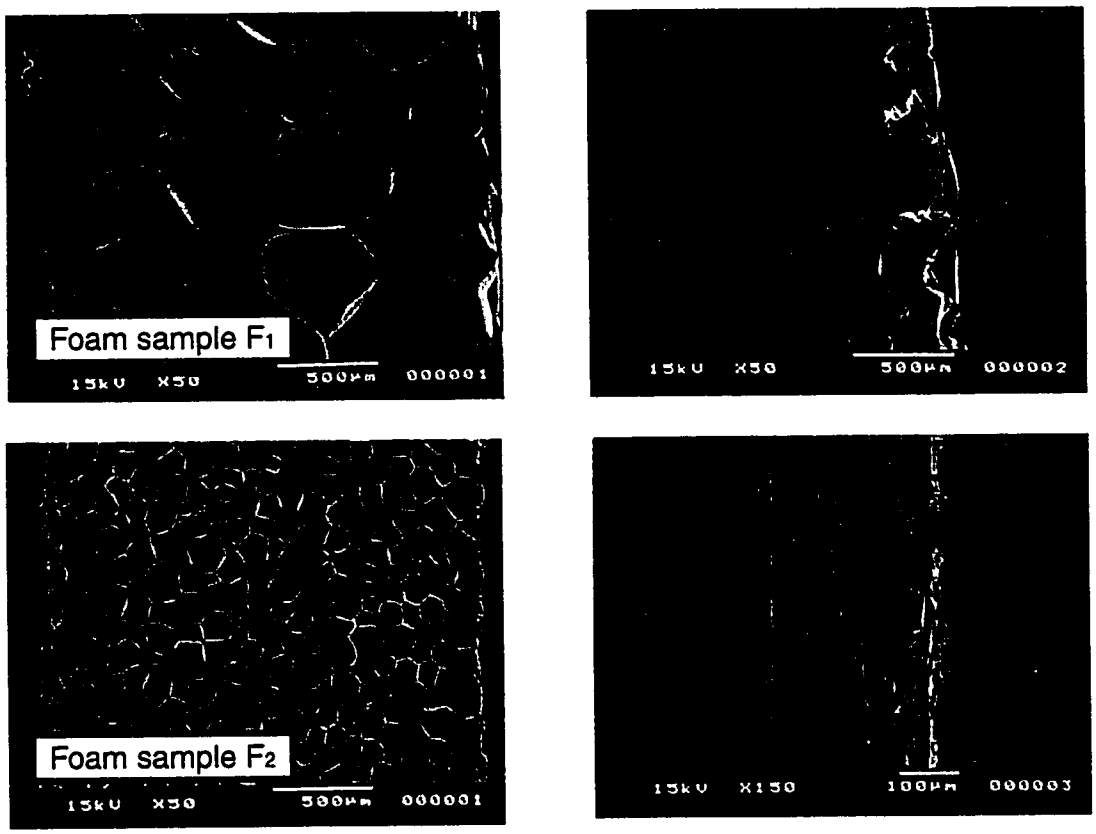

Figure 4.11 Microstructure of uncompressed and compressed foam sample F_1 and F_2

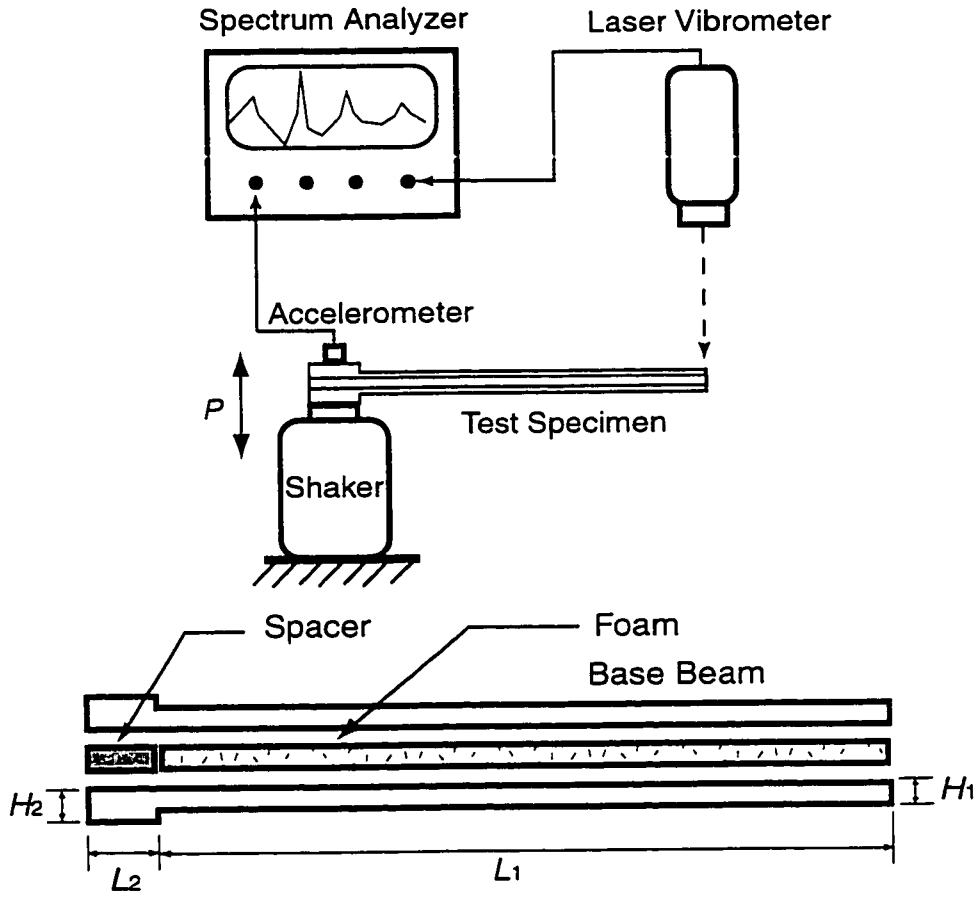

Figure 4.12 Test system and the specimen

Table 4.2 Configurations of the specimen

Specimen	Materials	Length (mm)	Thickness(mm)	Width (mm)
Root	Aluminum	$L_2 = 33.5$	$H_2 = 4$	10
Base beam	Aluminum	$L_1 = 220$	$H_1 = 2$	10
Spacer	Aluminum	33.5	varying	10
Foam	PETG foam	220	varying	10

examined. In our tests, the errors of the FRFs of the two base beams are under 0.8% for all modes.

In order to determine how well the boundary conditions of the fixed end are, the loss factors for untreated base beams were evaluated. The loss factors for the base beams are 0.003% for the first and second mode and 0.001% for the higher modes. The results are very similar to the ASTM standard for steel beams. Figure 4.12 shows a schematic drawing of the system and the specimen. In the ASTM standard, the apparatus consists of a rigid fixture to clamp the specimen and an exciter transducer such as the non-contacting electromagnetic type is used to generate the excitation force. Usually, when a non-contacting type exciter is used, it will cause a static force on the beam and result in some static deformation of the beam, which causes uneven preload on the damping material. This is true if the static force has a component in the axial direction of the specimen. In this case, the natural frequencies of the specimen might be affected.

To avoid possible errors from this apparatus, we used a shaker to excite the specimen (as we used in our previous projects). A signal generator powers the shaker with Gaussian broadband noise. Two transducers are utilized. To minimize extraneous sources of damping, a non-contacting type transducer such as a laser vibrometer is used to measure the response of the specimen's free end. An accelerometer is mounted at the base beam's cantilevered end to measure the excitation of the specimen's cantilevered end. Both the laser vibrometer and the accelerometer were connected to a spectrum analyzer for computing FRFs.

The ambient temperature was maintained at 73°F. We observed and recorded the FRFs of the first seven modes (0-5k Hz). In order to obtain high resolution of the FRFs, the zoom function was set, and the average times for signals collection was set to be 20 times. The FRFs were obtained by computing the transfer function between the vibrometer and accelerometer outputs. After the FRFs of each mode were obtained, the resonant frequency and half-power bandwidth can be computed.

4.2.3 Results and Discussions

In order to determine if our test system is well calibrated, two PETG foams with same density but different foam thickness are tested. Our test results show that regardless of the thickness of the damping layer, the same results of shear modulus and loss factor are obtained. Figure 4.13 shows the test results from PETG foam with thickness of 1.62 mm (foam F_2) and 3.24 mm (foam F_3). The results we obtained from this test are very consistent. This means that our system is stable and not affected by the thickness of the damping layer and the effect of the adhesive used to assemble the foam to the base beam.

Figure 4.14 shows the shear storage modulus and loss factor of five PETG foams with different densities (foam F_2, F_4, F_5, and F_6). The results show that microcellular foam with higher density has larger shear modulus. The range of the loss factor value varies from 3% to 7% and it does not seem have a direct relationship to foam density.

Figure 4.15 shows the results of PETG foam with density 40 kg/m^3 (foam F_2). We compared the shear modulus and loss factor of uncompressed, compressed and partially compressed foam. The CTR of the partially compressed foam is 60% which means that the bubbles in the foam are not fully collapsed. Note that neither the shear modulus nor the loss factor of the PETG compressed foam is higher than that of the uncompressed foam. The results of partially compressed foam are located between the results obtained from the uncompressed foam and the fully compressed foam. It indicated that the more we compressed the foam, the worse the damping becomes.

In order to evaluate if the same results apply to other PETG foams, PETG foam with density 150 kg/m^3 (foam F_5) was also evaluated. Figure 4.16 shows the same results that compressed foam does not improve the damping. From the microstructure of the compressed foam, we can observe that the cells of the voids are squeezed and very damaged. This may be the reason that caused the compressed foam to have lower shear modulus. Also, it may be necessary to apply a preloaded force on the compressed foam to induce the friction during the shear deformation in order to have lower loss factor.

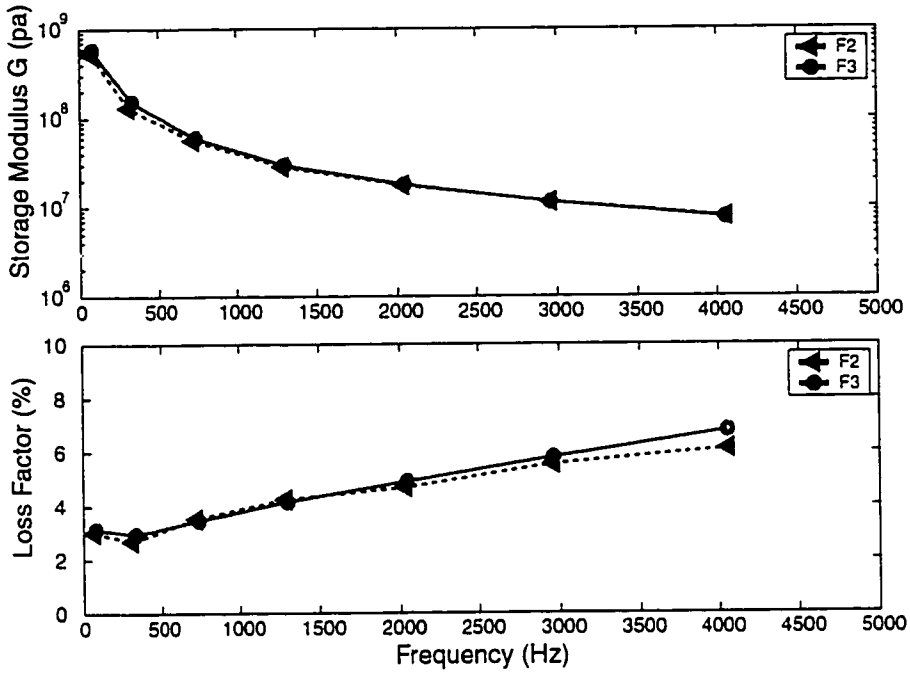

Figure 4.13 Shear modulus and loss factor of F2 and F3

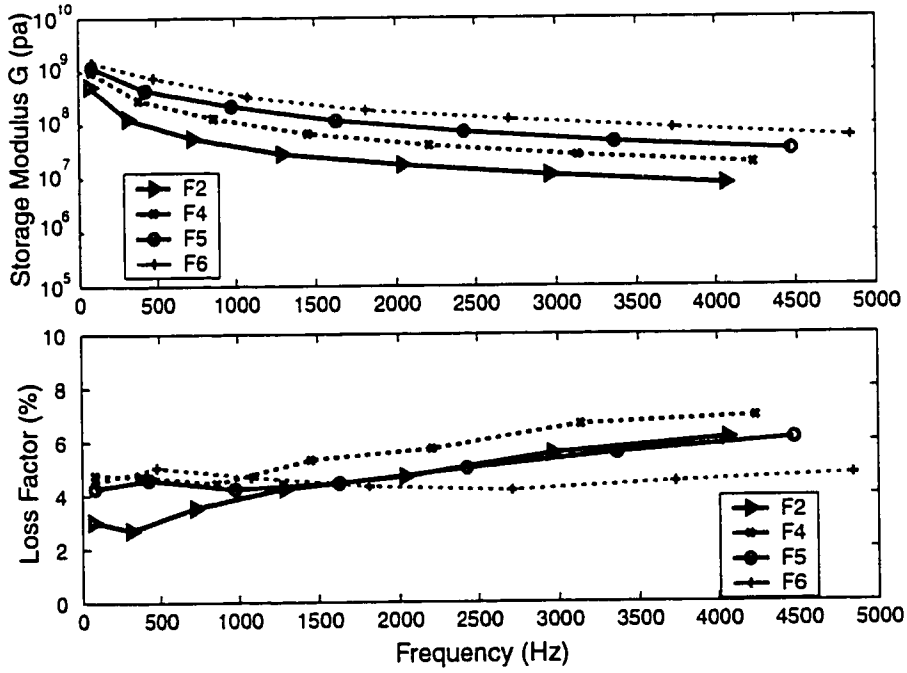

Figure 4.14 Shear modulus and loss factor of different foam

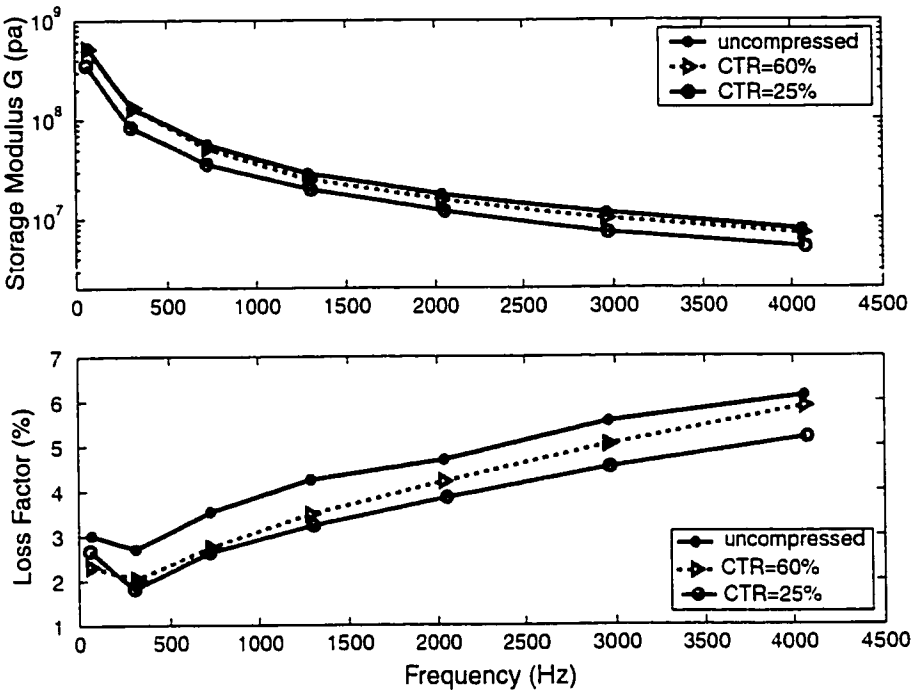

Figure 4.15 Shear modulus and loss factor of uncompressed and compressed F_2

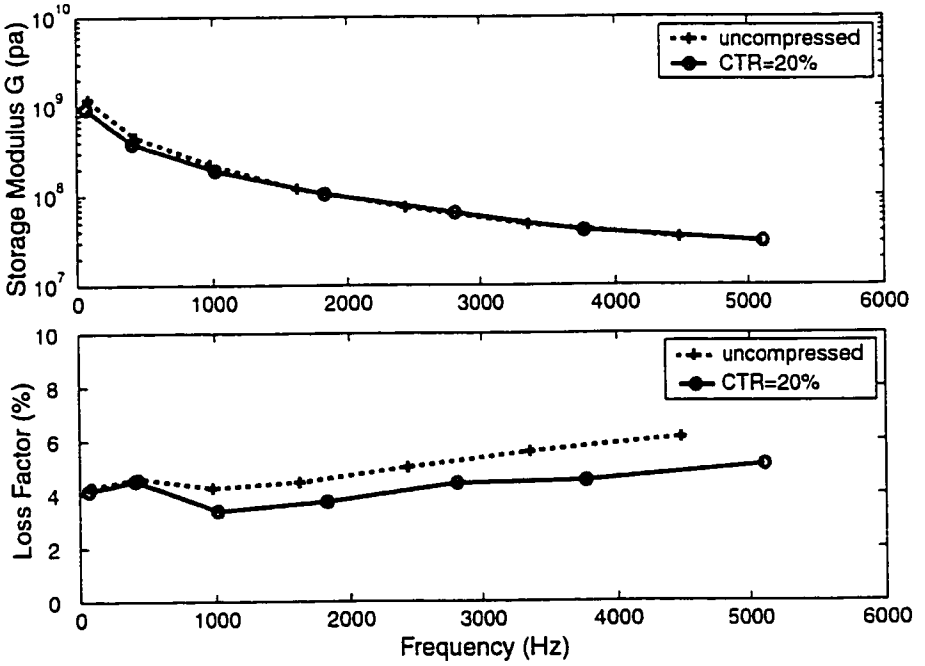

Figure 4.16 Shear modulus and loss factor of uncompressed and compressed F_5

To evaluate if PETG microcellular foam may be useful for damping, we compared the results we obtained with the shear modulus and loss factors of ISD 112 (a widely used damping material in the industry). The data of ISD112 were also obtained by using our test system. Figure 4.17 shows that PETG foam F_2 has higher shear modulus in low frequency range. However, the loss factor of ISD 112 rangs from 103.6% to 136% and is much higher than that of the PETG foam. We can see that PETG microcelluar foam is not a suitable damping material.

4.3 Microcellular Foam as Standoff Layer in CLD

In this section, we evaluate the possibility of using microcellular foam as a standoff layer in CLD. The principle of standoff CLD is first introduced. The experimental method is then described and followed by our test results.

4.3.1 Principles of Standoff CLD

Standoff CLD was first proposed by Whitter in 1959 [25]. In standoff CLD, a standoff layer is inserted between the base beam and the damping layer. The standoff layer moves the damping and constraining layer farther from the neutral axis of the vibrating structures, thereby increasing the shear angle of the damping layer and increases its energy dissipation. A good candidate for the standoff layer should have greater shear stiffness than that of the damping layer [26] and has low density to minimize the weight penalty. Foam has both the characteristics of high shear modulus and low density, making it a good candidate for use as standoff layer. In this section, we evaluate the possibility of using microcellular foam as a standoff layer in CLD.

4.3.2 Experimental Setup and Procedures

Except the specimen, the experimental setup to obtain the transfer function of the beam is similar to the measurement system as described in the previous section. We used one of the base beams in our measurement system described in the previous section. The commercial CLD tape consisting of a layer of very thin ISD 112

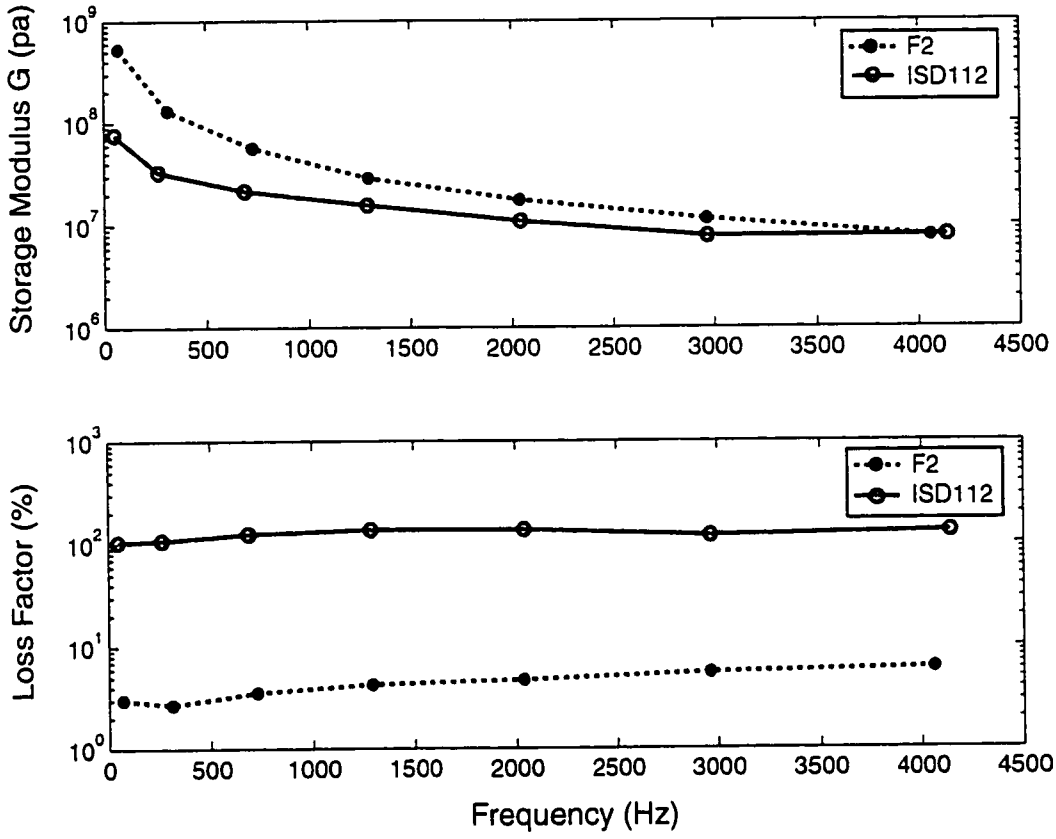

Figure 4.17 The comparison of ISD 112 and F_2

viscoelastic (0.13 mm thickness) and a layer of aluminum foil (0.2 mm thickness) was used in the specimen. Two foams with densities 42 kg/m^3 (F_3) and 100 kg/m^3 (F_4) were applied as the standoff layer between the base beam and the CLD tape in the specimen. The first seven modes in the frequency range from 0 Hz to 5k Hz were obtained. In order to evaluate how partially treated standoff CLD has equivalent damping as fully treated CLD without standoff, different sizes of treatments applied to the center of the base beam was also investigated. We recorded the amplitude of FRFs and used half-power method to calculate the loss factor for each mode of the specimen.

4.3.3 Results and Discussions

Figure 4.18 shows the comparisons of FRFs for specimens with and without standoff layer. It shows that the amplitudes of seven modes have been reduced significantly if the specimens were additionally treated with standoff layer. In Table 4.3, it can be seen that amplitude reduction for specimen B can reach up to 74% for the second mode with a 2% weight penalty. For the higher modes, the amplitude reduction is around 30% to 45%. Specimen C has better performance than specimen B for all modes. Although the standoff layer used in specimen B is foam F_3 that has thicker thickness than that of foam F_4 in specimen C, however, foam F_4 has greater shear modulus than that of foam F_3.

The loss factors of the specimen with different sizes of partially treated standoff CLD were evaluated. Table 4.4 shows some experimental results. Note that specimen B with 70 % partially treated standoff CLD and specimen C with 60 % partially treated standoff CLD have equivalent loss factors of fully treated CLD beam (without standoff layer) for mode 1. For the other modes, we see that smaller size of standoff CLD can reach the equivalent loss factor. In the other words, by adding a very light standoff layer, we can effectively decrease the required size of the CLD treatment and still obtain the same result of vibration control as when fully treated CLD is used.

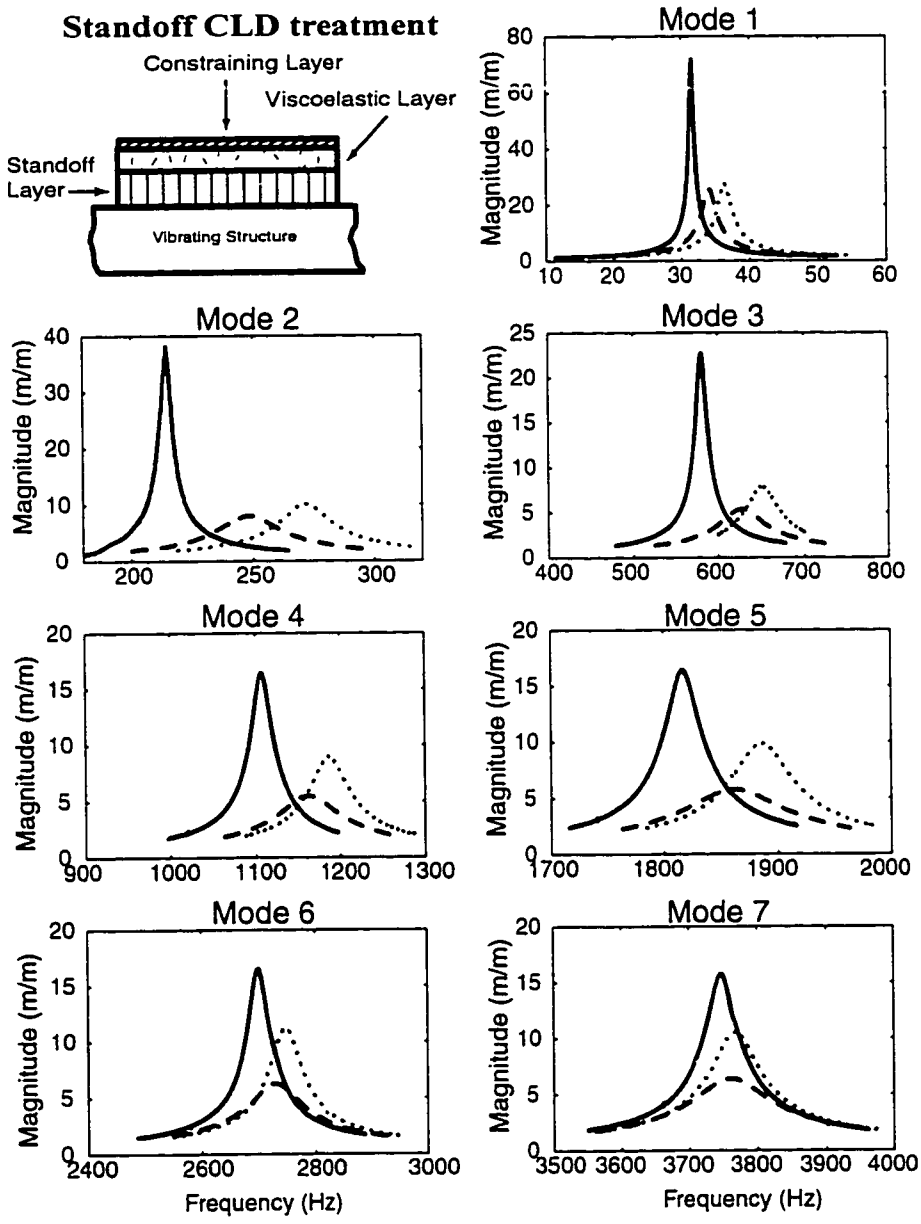

Figure 4.18 Comparison of FRFs of CLD and standoff CLD

Table 3. The comparisons of FRFs' amplitude of specimens with and without standoff layer

No	Standoff Materials		Mode 1	Mode 2	Mode 3	Mode 4	Mode 5	Mode 6	Mode 7	Weight Penalty
A	None		71	38.19	22.67	16.42	16.42	16.51	15.7	0%
B	F_3	Amplitude	27.47	10.10	7.86	9.0	9.88	11.21	10.53	2%
		Reduction	63%	74%	65%	45%	40%	32%	33%	
C	F_4	Amplitude	25.54	8	5.34	5.47	5.78	6.27	6.36	3%
		Reduction	64%	79%	76%	67%	65%	62%	60%	

Table 4. The comparisons of loss factors of specimens with partially treated standoff layer CLD

No	Standoff Materials	Treatment (%)	Loss factor (%)						
			Mode 1	Mode 2	Mode 3	Mode 4	Mode 5	Mode 6	Mode 7
A	None	100	1.07	0.99	1.03	1.04	0.81	0.66	0.58
B	F_3	100	2.73	3.74	2.73	1.83	1.31	0.96	0.89
		70	1.09	3.28	1.66	1.05	0.81	0.65	0.54
		60	0.80	2.57	1.03	0.97	0.78	0.55	0.40
C	F_4	100	2.98	4.89	4.12	3.06	2.26	1.63	1.49
		70	1.23	4.29	2.31	1.48	1.16	1.01	0.93
		60	0.93	3.37	1.66	1.46	1.20	1.00	0.69
		50	0.70	3.14	1.04	1.41	1.15	0.72	0.59

These results become very helpful in some industry such as aerospace industry where weight reduction is needed.

4.4 Conclusions

1. Test results show that damping of PETG microcellular foams ranges from 2% to 8% and is independent of foam density and thickness.
2. A thermal cycling method is developed to compress the foams and collapse the bubbles.
3. Compressed foams do not present a large damping compared with uncompressed foams
4. Using microcellular foam as standoff layer can reduce vibration by 80% with only 2% weight penalty.

Chapter 5

CONCLUSIONS

5.1 Summary of Contributions from Current Research

In our research, we first investigated the limitations of the Mead-Markus model theoretically and experimentally. We concluded that careful attention to the boundary conditions must be exercised when predicting the behavior of the first mode using the Mead-Markus model. For certain boundary conditions, more accurate results can be obtained by using the MMM model.

We further expanded our research in chapter 2 by considering the thickness deformation of the viscoelastic layer in CLD. We proposed a technique that allows direct measurement of thickness deformation in CLD treatment. This direct measurement technique is feasible and can detect thickness deformation with relative thickness deformation (RTD) as low as 0.5%. The experimental results show that for the fully treated CLD beam, RTD increases as frequency increases. In addition, RTD increases as thickness of the viscoelastic layer increases. We also found that partially treated CLD beams tend to have larger thickness deformation than fully treated beams. When thickness deformation becomes noticeable, the TD model predicts FRFs better than the MMM model.

In our first two research topics, we analytically and experimentally verified the validity of the models for CLD beam. It seems that the TD model is the best model to use for predicting the behavior of CLD beam. However, due to the complexity of the equations of motion, the computation of the TD model is very complicated. It is not necessary to use this model if the thickness deformation of the viscoelastic layer is not considerable. Using this model in the development of other innovative CLD beam models such as standoff layer CLD or some active CLD may result in intricate equations of motion and increase the difficulty to compute the FRFs. For the same

reason, if the boundary conditions do not violate the assumptions as introduced in chapter 2, the Mead-Markus model remains a simple yet relatively accurate method for predicting the behavior of CLD beam, because the Mead-Markus model has only one equation of motion.

In chapter 4, two feasibility studies were conducted using microcellular foam in CLD applications to take advantage of its low density. Results of the feasibility studies show that the loss factor of PETG foam with densities from 42 kg/m^3 to 240 kg/m^3 is in the range of 2% to 8%. In addition, there is no significant difference in loss factor between the uncompressed and compressed foams. Also, use of microcellular foam as standoff layer can reduce vibration amplitude up to 80% with only a 2 % to 3% weight penalty.

5.2 Future Work

1. In the thickness deformation of CLD study, our experimental results show that the partially treated beam has more significant RTD than that of the fully treated beam. This research work can be extended with theoretical analysis and verification of the experimental results.
2. The thickness deformation effect was only investigated in the one-dimensional condition. It will be interesting to observe the thickness deformation effect in the two-dimensional condition.
3. We developed a method to compress foam materials and collapse the bubbles. Our original motivation was to verify our assumption that compressed foam can increase damping effects. However, we did not see any improvement. Our technique can close bubbles in the microstructure foam and compressed the foam up to 20 % thickness. This technique may be useful for other applications requiring compressed foam.
4. Microcellular foam has high potential to be used as standoff layer in CLD treatments. In this paper, we only evaluated the PETG foam. This work can be extended to include different types of foam. Another possible research area

is the investigation of the optimum foam density for standoff layer. The goal is to create foam with bigger bubble size without sacrificing the shear modulus.

BIBLIOGRAPHY

[1] Mead, D. J. and Markus, S., 1969, "The Forced Vibration of a Three-Layer Damped Sandwich Beam with Arbitrary Boundary Conditions," *Journal of Sound & Vibration*, Vol. 10 (2), pp. 163-179.

[2] Swallow, W., 1939, "An Improved Method of Damping Panel Vibrations," *British Patent Specification* 513, 171.

[3] Ross, D., Ungar, E., and Kerwin, E. M., 1959, "Damping of Plate Flexural Vibrations by Means of Viscoelastic Laminae," *Structural Damping*, Proceedings ASME Colloquium on Structural Damping, pp. 49-88.

[4] DiTaranto, R. A., 1965, "Theory of the Vibratory Bending for Elastic and Viscoelastic Finite Length Beam," ASME *Journal of Applied Mechanics*, Vol. 32, pp. 881-886.

[5] Mead, D. J., 1965, "The Effect of Certain Damping Treatment on the Response of Idealized Aeroplane Structures Excited by Noise," *Air Force Materials Lab.*, AFML-TR-65-284 WPAFB.

[6] Trompette, P., Boilot, D., and Ravanel, M. A., 1978, "Effect of Boundary Conditions on the Vibration of a Viscoelastically Damped Cantilever Beam," *Journal of Sound and Vibration*, Vol 60 (3), pp. 345-350.

[7] Shen, I. Y., 1994, "Hybrid Damping Through Intelligent Constrained Layer Treatments," ASME *Journal of Vibration and Acoustics*, Vol. 116, pp. 341-349.

[8] Miles, N. R, and Reinhall, P. G., 1986, "Analytical Model for the Vibration of Laminated Beams Including the Effects of Both Shear and Thickness Deformation in the Adhesive Layer," ASME *Journal of Vibration, Acoustics, Stress, and Reliability*, Vol. 108 (1), pp. 56-64.

[9] Douglas, B. E. and Yang, J. C. S., 1978, "Transverse Compressional Damping in the Vibratory Response of Elastic-Viscoelastic-Elastic Beams," *AIAA Journal*, Vol. 16, No. 9, pp. 925-930.

[10] Douglas, B. E., 1986, "Compressional Damping in Three-Layer Beams Incorporating Nearly Incompressible Viscoelastic Cores," *Journal of Sound and Vibration*, Vol. 104, No. 2, pp. 343-347.

[11] Sylwan, O., 1987, "Shear and Compressional Damping Effects of Constrained Layer Beams," *Journal of Sound and Vibration*, Vol. 118 (1), pp. 35-45.

[12] Chen, Y. H. and Sheu, J. T., 1994, "Dynamic Characteristics of Layered Beam with Flexible Core," ASME *Journal of Vibration and Acoustics*, Vol. 116, pp. 350-356.

[13] Austin, E. M. and Inman, D. J., 1997 "Studies on the Kinematic Assumptions for Sandwich Beams," *Passive Damping and Isolation*, Proceedings SPIE Smart Structures and Materials, Vol. 3045, pp. 173-183.

[14] Baz, A., Imam, K, and McCoy, J. 1990, "Active Vibration Control of Flexible Beams Using Shape Memory Actuators," Journal of Sound and Vibration v 140 (3), pp. 437-456

[15] Liao, W.H., and Wang, K.W.,1997, "On The Analysis of Viscoelastic Materials For Active Constrained Layer Damping Treatments," *Journal of Sound and Vibration*, Vol. 207 (3) pp. 319-334

[16] Yang, B. and Tan, C. A., 1992, "Transfer Function of One-Dimensional Distributed Parameter System," ASME *Journal of Applied Mechanics*, Vol. 59, pp. 1009-1014.

[18] Lee, Nathaniel T. 1998, "Sound Absorption Behavior of PETG Microcellular Foams," *Master thesis*, University of Washington.

[19] Sharon, L. Eddy, 1996, "Solid-state PETG Foams," *Master thesis*, University of Washington.

[20] Markus, S., Oravsky, V., and Simkova, O., 1974," Damping Properties of Sandwich Beams with Local Shearing Prevention," *Acustica*, Vol. 31, pp. 132-138.

[21] Rao, D. K., 1978, "*Frequency and Loss Factors of Sandwich Beams under Various Boundary Conditions*," Journal Mechanical Engineering Science, Vol. 20 No. 5, pp. 271-282.

[22] Lifshitz, J. M. and Leibowitz, M., 1987, "Optimal Sandwich Beam design for Maximum Viscoelastic Damping," *International Journal of Solid Structures*, Vol. 23, No. 7, pp. 1027-1034.

[23] Soovere, J. and Drake, M. L., 1985, *Aerospace Structures Technology Damping Design Guide Vol. III - Damping Material Data,* AF Wright Aeronautical Laboratories, Ohio.

[24] American Society for Testing and Materials, 1998, "Standard for Measuring Vibration Damping Properties of Materials, E756-80," ASTM.

[25] Whittier, J. S., 1959, "The Effect of Configurational Additions Using Viscoelastic Interfaces on the Damping of a Cantilevered Beam,", *WADC Technical Report* 58-568, Wright Air Development Center.

[26] Mead, D. J. 1999, *Passive Vibration Control*, pp. 409, Wiley, London.

VITA

Yao-Hsin Huang

EDUCATION

University of Washington, September 1996 - August 2000

Ph.D., Mechanical Engineering

University of Utah, September 1994 - August 1996

M.S., Mechanical Engineering

Feng Chia University – Taiwan, September 1986 - June 1990

B.S., Mechanical Engineering

PUBLICATIONS

1. Huang, Peter Y. H., Reinhall, Per G., Shen, I. Y., and Yellin, J. M., "Thickness Deformation of Constrained Layer Damping: An Experimental Evaluation," Accepted for publication in ASME Journal of Vibration and Acoustics.
2. Huang, Peter Y. H., Reinhall, Per G., and Shen, I. Y., "Constrained Layer Damping Models under Clamped Boundary Conditions," Accepted for publication in ASME Journal of Vibration and Acoustics.
3. Yellin, J. M., Reinhall, Shen, I. Y., and Huang, Peter Y. H. "Vibration analysis of passive astandoff constrained layer damping treatments," accepted for publication in ASME Journal of Vibration and Acoustics.
4. Huang, Peter Y. H., "An Improvement of A System to Determine the Sound Exposure to the Person Wearing Headsets," Master Thesis, University of Utah, Dec. 1996.